Report to Baoshan Iron and Steel Co., Ltd.

Prediction of Hot Tearing Cracks during High-Alloy Continuous Casting at Baosteel

Brian G. Thomas

University of Illinois at Urbana-Champaign

Mechanical Science and Engineering

University of Illinois at Urbana-Champaign

Chengbin Li

Metallurgical Process Institute

R&D Center, Baosteel

Feb. 7, 2010

1. Introduction

1.1. Background

Following the Frame Agreement between UIUC and Baosteel signed in 2005, this project is the first step to begin a cooperative research effort.

Continuous casting of large section blooms of high-alloy steel is an important new direction for Baosteel. Specifically, Baosteel has commissioned a new 320mm*425mm bloom caster in Fall of 2007, with high-alloy steel as one of the main products. As Baosteel always aims to produce high-quality steel, attention to internal quality is essential. This process and product is particularly susceptible to internal cracks caused by hot tearing. Thus, the following research project was undertaken to improve understanding of the formation of hot tear cracks in high-alloy grades, in order to facilitate fast diagnosis and solution of any internal cracking problems that arise in the future. The project should be a starting point, towards the ultimate ability to predict and prevent internal quality problems in a quantitative manner.

The Principal Investigator, Professor B.G. Thomas has a great deal of research experience in the prediction of internal quality problems in continuous casting, particularly through the application computer simulation. With the help of Baosteel, including laboratory measurements, plant data, and efforts of visiting researchers, it is hoped that this project will improve research collaboration between these two institutions, in addition to increasing knowledge and research tools for minimizing this important internal quality problem.

1.2. Objectives

1) Improve understanding of the cause of internal quality problems in continuous casting of steel, particularly the mechanism of hot tear crack formation in high-alloy bloom casters.

2) Develop an off-line computational model, which can simulate thermal and mechanical behavior in the continuous-cast steel shell, including prediction of temperature, displacement, stress, and a criterion for hot-tear crack formation.

3) Apply this model to investigate the mechanism of hot tear crack formation, and to predict the location of such cracks relative to the distance of casting problems such as roll misalignment down the casting machine.

1.3. Methodology

Slices through the solidifying steel shell have been modeled at UIUC to predict temperature, microsegregation, displacement, stress, and hot-tear cracks, with the help of experimental measurements obtained from Baosteel. The details are reported in the following steps.

1.3.1.   Literature Review

The important knowledge about hot-tear crack formation in high-alloy bloom continuous casting from previous work are investigated first.

1.3.2.   Modeling of heat transfer and solidification

The model is then applied to obtain the temperature distribution in a 1-D, 2-D section or 3d one-layer section through a typical bloom. It is based on existing models developed in the Continuous Casting Consortium to solve the transient heat conduction equation with solidification in continuous cast steel, including CON1D and a user-customized version of ABAQUS.

The model is also used to output the micro segregation profile expected as a function of distance beneath the steel surface (neglecting fluid flow effects).   The calculation will be based on diffusion of alloying elements in the interdendritic liquid developed in previous work.

1.3.3.   Stress analysis

Next, a thermal-stress model has been used to solve the equilibrium, constitutive, and compatibility equations using the finite element method to compute the mechanical behavior of the solidifying shell.   The model incorporates realistic elastic-viscoplastic, phase- and temperature-dependent constitutive equations that include the known variations with stress, strain-rate, and steel-grade. Other properties are taken to be temperature-dependent as well.   The stress state of generalized plane strain is assumed in order to achieve three-dimensional accuracy even with a slice model domain.

1.3.4. Hot tear prediction

A criterion is used to estimate hot tearing, based on the inelastic strain accumulated during the final stages of solidification of the mushy zone of the shell. The model can be applied to simulate hot-tear crack formation development during solidification, and can answer questions such as: do hot tears begin near the surface and propagate inward, or propagate the other way towards the surface? What is the relation between the location of the crack and the solidification front?   To model radial streak hot tears, bending and unbending, and roll misalignment, thermal stress, and bulging of the shell will be taken into account.   To model longitudinal cracks, the computation focuses on thermal stress, especially in the mold region.   The exact nature of the cracks to model is based on the findings of the literature and expectations of the most important problems from Baosteel, such as centerline cracks.

1.3.5. Experimental Measurements

In support of this modeling, in order to make the predictions as quantitative as possible, Baosteel should provide the following information:
- continuous casting machine data and casting conditions
- steel chemical composition(s) of interest
- steel thermal properties, including liquidus temperature, solidus temperature, and phase fractions as a function of temperature for the alloys of interest.
- measurement of the high-temperature mechanical properties of selected steel grades, including the complete load-displacement histories (raw data measured), and the complete geometry and conditions of the laboratory experiments
- heat transfer coefficients for the caster, and the details of the raw experimental measurements used to obtain them
- experiments to measure crack formation during solidification for validation of the hot-tear crack criteria

When available, micrographs and casting conditions for any internal hot tear cracks that form in the actual caster

1.3.6. Verification and Model Calibration

The next stage of the work is to validate the model predictions using the best available plant data from Baosteel. Variables to consider comparing with measurements include: surface temperature, final solidification point, and the location of cracks in the product.

1.4. Schedule

This project will be finished in 2 years (06/08 to 05/10)
06/25/2008-08/25/2008   Literature survey
06/25/2008-06/25/2009   Model development; Submit a progress report
06/25/2009-12/24/2009   Verify and Calibrate model; Test model to predict the actual process.
12/24/2009-05/24/2010   Final report

2. Literature Review

Crack formation has long been recognized as a problem in the continuous casting of steel. Cracks have been observed at almost every conceivable location in cast steel sections as shown schematically in Fig Error**! Reference source not found.**.1[1]. In the interior, cracks may be seen near the corners, at the centerline or diagonally between opposite corners. On the surface, transverse and longitudinal cracks may appear in both the mid-face and corner regions.
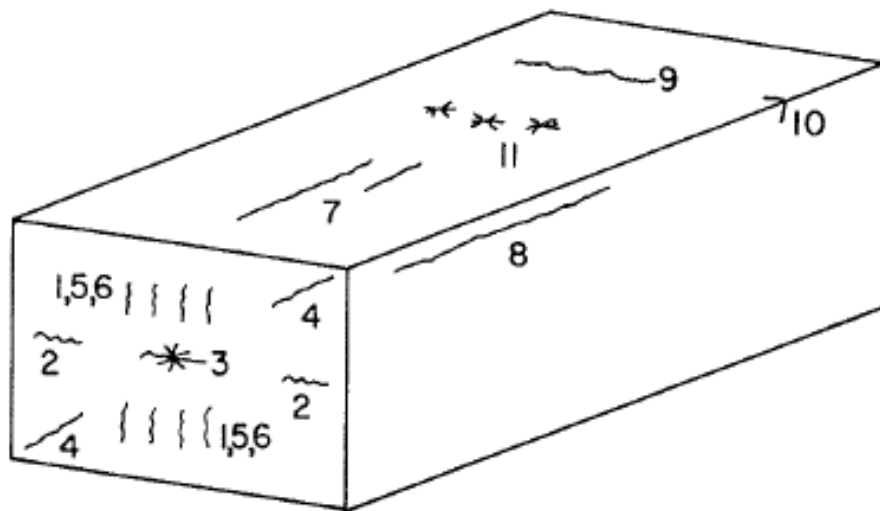
Cracks in continuously cast steel
Internal cracks
1 Midway
2 Triple-point
3 Centerline
4 Diagonal
5 Straightening/bending
6 Pinch roll

Surface cracks
7 Longitudinal, mid-face
8 Longitudinal, corner
9 Transverse, mid-face
10 Transverse, corner
11 Star

Fig **Error! Reference source not found.**.1 Schematic drawing of strand cast section showing different types of cracks.

The reason for the profusion of crack types lies in the nature of the continuous casting process itself. The rapid cooling results in steep temperature gradients in the solid shell that can change rapidly and generate thermal strains as the shell expands or contracts Fig **Error! Reference source not found.**.1[,2,3]. In addition, because the semisolid section is required to move through the machine, it is subjected to a variety of mechanically induced stresses caused by friction in the mould, roll pressure, ferrostatic pressure, machine misalignment, bending and straightening operations Fig **Error! Reference source not found.**.1. Depending on their magnitude, any of these stresses and strains may result in crack formation.

Lankford has discussed the nature of the stresses and strains that can give rise to cracks in the solidifying shell[4]. Tensile force and expand strain may result in crack formation at low ductility zones.

There are three temperature zones where steel is susceptible to crack.

◆ High temperature zone: ~ 1340 C to solidus.
◆ Intermediate temperature zone: 800 C to 1200 C
◆ Low temperature zone: 700 C to 900 C

Above about 1340 C, the low strength and ductility seem to be due to the presence of liquid films in the interdendritic regions, which do not freeze until temperatures well below the solidus are reached[5],[6]. The liquid films apparently contain high levels of sulfur, phosphorus and other elements, which have a segregation coefficient less than unity and which concentrate between the growing dendrites.

In the intermediate temperature zone, the loss of ductility during cooling below 1200 C is strongly dependent on the Mn/S ratio and thermal history of the steel. Lankford has proposed a mechanism by suggesting that the low ductility results from the precipitation of liquid droplets of FeS in planar arrays at austenite grain boundaries, which are then paths of easy crack propagation. Lankford has further shown that slower cooling rates improve the ductility even with low Mn/S because manganese then has time to diffuse to the grain boundaries.

The third zone of low ductility is associated with soluble aluminum in the steel, the precipitation of AlN [7,8] and the pre-ferrite at grain boundaries[9].

The cause of a particular type of crack can be determined if the information concerning stresses and mechanical properties is combined with practical knowledge obtained from a continuous casting operation. From plant observations the location and orientation of the cracks can be ascertained, together with the operational factors

thought to cause and cure the cracks.

The information on internal cracks is summarized in Table **Error! Reference source not found.**.1.

Table **Error! Reference source not found.**.1 Internal Cracks

Type	Cause	Influencing Factors	Corrective Action
Midway Cracks	Surface reheating in or below spray chamber	High casting temperature, S and P>0.02 pct increase crack formation	Adjust spray system to minimize reheating. Lower pouring temperature, Minimize P and S levels
Triple-point Cracks	Bulging of wide face of slabs	Cracking increases with decreasing Mn below 0.9 pct Mn and with Mn/S<30	Regap rolls
Centerline cracks	In slabs, bulging of wide face	Spray water intensity, casting speed, roll alignment low in the strand	Regap rolls, reduce casting speed or increase spray cooling
	In billets, rapid cooling of center region below pool	Severe secondary cooling and high pouring temperature may enhance crack formation	Adjust secondary cooling near bottom of pool
Diagonal cracks	Asymmetrical cooling in mould or sprays	High pouring temperature and smaller billet sizes increase cracking	Install corner rolls at bottom of mould and roller apron. Look for plugged spray nozzles
Straightening/bending cracks	Excessive deformation near solidification front due to straightening or bending	Bending on liquid center	Reduce tensile strain at solidification front to less than 0.3 pct. Lower casting speed

Pinch roll cracks	Excessive pinch roll pressure	Squeezing on a liquid center	Reduce pinch roll pressure

All internal cracks form in high temperature zone of low ductility, between 1340 C and solidus temperature. Elements such as P, S and Cu worsen the crack problem.

A summary of information on surface cracks is given in Table Error**! Reference source not found.**.2.

Table **Error! Reference source not found.**.2 Surface Cracks

Type	Cause	Influencing Factors	Corrective Action
Longitudinal, midface cracks	Tensile strain generated in the mould and upper spray zones	Crack frequency increased by: --carbon levels of 0.12 pct --increasing S and Decreasing Mn/S --varying or increasing --casting with high pouring temperatures --casting wide slabs --mold conditions—improper water cooling, loss of taper, irregular mold oscillation, improper mold powder, worn molds --overcooling in upper spray zones --insufficient support below mold --poor alignment between mold and submold support system	Adjust mold conditions to ensure uniform cooling. Reduce cooling in upper spray zones and check submold system
Longitudinal, corner cracks	Nonuniform cooling in corner reion	Cracking associated with: --reversal of mold taper owing to distortion or wear --large corner gaps in plate molds --high tundish temperature	Plate mold walls with chromium. Reface the mold. Check alignment and lubrication for uniformity

		--high casting speed	
		--incorrect foot roller settings	
		--steel containing 0.17-0.25 pct C, S>0.035 pct, P>0.035 pct	
Transverse, midface and corner cracks	In slabs off-corner cracks caused by bulging of narrow face in mold	Long molds and steel with 0.15 to 0.23 pct C give rise to worse cracking	Check mold support conditions
	Large surface temperature gradients in the spray zone and straightening within an unfavorable range of temperature, between 700 and 900 C	Strongly influenced by steel composition, Al, V, Nb, Mn>1 pct being the most important elements	Reduce spray cooling and make as uniform as possible to minimize cooling/reheating cycles and maintain surface temperature above 900 C through to straightener
Star cracks	Scraping of copper from mold	Secondary cooling	Plate mold walls with chromium. Adjust machine alignment
With the exception of transverse cracks, surface cracks probably form in the high temperature zone of low ductility			

3. Modeling of Heat Transfer and Solidification

3.1. Previous work

Heat transfer in the continuous casting process is governed by many complex phenomena. Many mathematical models have been developed of the continuous casting process. The earliest solidification models used one-dimensional finite-difference methods to calculate the temperature field and growth profile of continuously cast steel shell.[10,11] Many industrial models followed. [12,13]These models first found application in the successful prediction of metallurgical length, which is also easily done by solving the following simple empirical relationship for distance (z) with the shell thickness (S) set to half the section thickness: $S=K(z/V_c)^{1/2}$

where K is found from evaluation of breakout shells and computations. Such models found further application in troubleshooting the location down the caster of hot-tear cracks initiating near the solidification front [14]and in the optimization of cooling practice below the mold to avoid subsurface longitudinal cracks due to surface reheating.[15]

Since then many advanced models have been developed to simulate further phenomena such as thermal stress and crack-related defects[16,17,18] or turbulent fluid flow coupled together with solidification[19],[20]. For example, a two-dimensional transient, stepwise coupled elasto-viscoplastic finite-element model tracks the behavior of a transverse slice through a continuously cast rectangular strand as it moves down through a mold at casting speed. This model is suited for simulating longitudinal phenomena such as taper design,[21] longitudinal cracks, [22] and surface depressions. [23] Other casters have been modeled using three-dimensional coupled fluid flow-solidification models based on control-volume or finite-difference approaches, at the expense of greater computation time and memory.

3.2. Con1d model

The CON1D program has been developed in the Metals Process Simulation Laboratory at the University of Illinois under the direction of Professor Brian G. Thomas. CON1D is a Fortran program which models heat transfer and solidification in the mold region of a continuous caster. The model simulates one-dimensional transient heat transfer-solidification in the steel shell coupled with 2-D steady-state heat conduction in the mold. Hence, the model is most easily applied to regions away from the corners of the cross-section. It is intended for the study of steel slab casters, but can also be applied to other processes.

The heat flux extracted from the solidified shell surface can either be supplied as a specified function of distance below the meniscus, or can be calculated using the interfacial model included in the program. The superheat can be treated in three different ways in the program: 1) calculating temperature in the liquid steel; 2) supplying a superheat flux profile as a stepwise linear function of distance below the meniscus; or 3) letting the program calculate the heat flux added to shell surface, based on previous 3-D turbulent flow calculations. The program can simulate wide/narrow face, outer/inner face of molds (with or without curvature). It is also capable of calculating heat transfer as the strand passes by each roll in the spray zones beneath the mold.

A large quantity of information can be obtained using CON1D, which runs in only a few seconds on a personal computer. The output results include the following variables (as a function of distance below the meniscus):

(1) Temperatures: mold hot face, cold face, shell surface and shell interior, cooling water

(2) Shell thickness (including positions of liquidus, solidus, and shell isotherms);

(3) Heat flux leaving the shell (across the interfacial mold / shell gap);

(4) Thickness and velocity of solid and liquid flux layers in the mold/shell interfacial gap;

In addition, the model derives important constants (solidus temperature, liquidus temperature, etc.) with micro segregation model.

A. Superheat Flux

Before it solidifies, the steel must first cool from its initial pour temperature to the liquidus temperature.   Due to turbulent convection in the liquid pool, the "superheat" contained in this liquid is not distributed uniformly.   A small database of results from a 3-D fluid flow model**Error! No bookmark name given.**$^{Error! No bookmark name given.}$ is used to determine the heat flux delivered to the solid / liquid interface due to the superheat dissipation, as a function of distance below the meniscus.   Examples of this function are included in Fig **Error! Reference source not found.**.1,[24] which represents results for a typical bifurcated, downward-directing nozzle.   The initial condition on the liquid steel at the meniscus is then simply the liquidus temperature.

The influence of this function is insignificant to shell growth on most of the wide face, where superheat flux is small and contact with the mold is good.
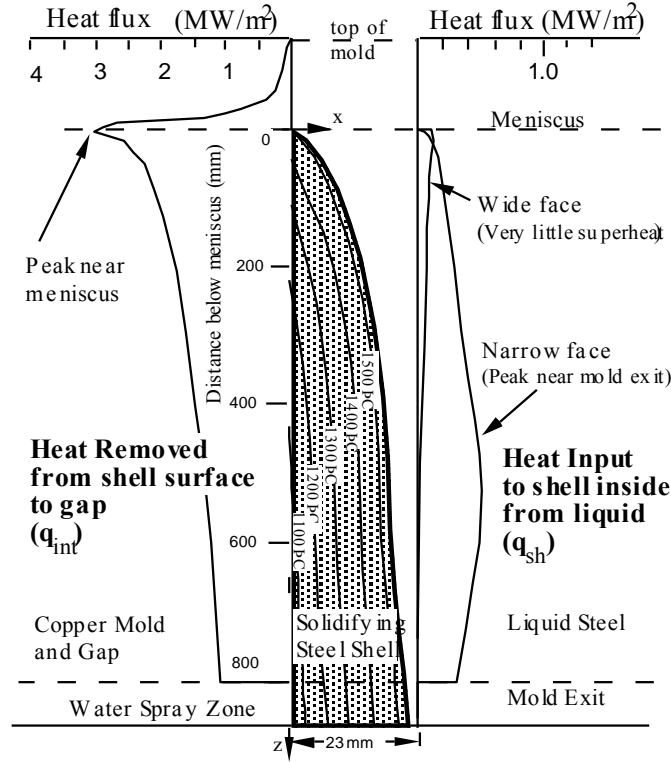
Fig **Error! Reference source not found.**.1 Model of solidifying steel shell showing typical isotherms and heat flux conditions

B. Heat Conduction in Solidifying Steel Shell

Assuming that axial heat conduction is negligible in the steel, which is reasonable due to the large advection component as indicted by the large Peclet number. Temperature in the solidifying steel shell is governed by the 1D transient heat conduction equation :

$$\rho_{steel} Cp^*_{steel} \frac{\partial T}{\partial t} = k_{steel} \frac{\partial^2 T}{\partial x^2} + \frac{\partial k_{steel}}{\partial T} \left(\frac{\partial T}{\partial x} \right)^2$$

[3.1]

where C_p^* , the effective specific heat for the solidifying steel, is defined as:

$$C_p^* = \frac{dH}{dT} = C_p - L_f \frac{df_s}{dT}$$

[3.2]

The simulation domain, a slice through the liquid steel and solid shell, together with the boundary conditions, is presented in Fig **Error! Reference source not found.**.1.

13

C. Heat Flux Across the Interfacial Gap

Heat flux extraction from the steel is governed primarily by heat conduction across the interfacial gap, whose thermal resistance is determined by the thermal properties and thicknesses of the solid and liquid powder layers, in addition to the contact resistances at the flux / shell and flux / mold interfaces and powder porosity, which are incorporated together into a single equivalent air gap, d_{air}. Slag consuming follows mass and momentum balance. Non-uniformities in the flatness of the shell surface, represented by the oscillation marks, have an important effect on the local thermal resistance, and are incorporated into the model through the depth and width of the oscillation marks. This is used to calculated an effective average depth of the marks relative to heat flow, d_{eff}. The oscillation marks can be filled with either flux or air, depending on the local shell temperature. When the gap is large, significant heat is transferred by radiation across the semi-transparent flux layer. This model for gap heat conduction is illustrated in Fig **Error! Reference source not found.**.2 and Fig **Error! Reference source not found.**.3 and given by the following
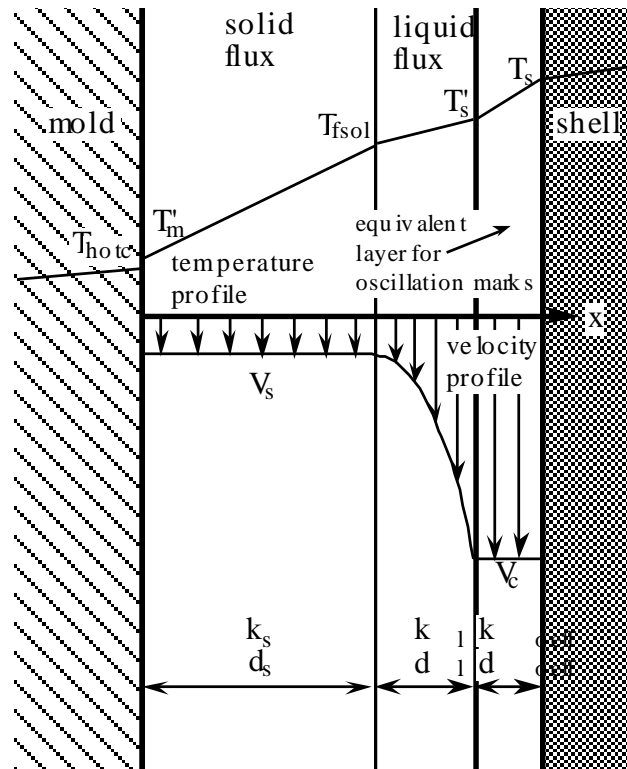
equation:

Fig **Error! Reference source not found.**.2 Velocity and temperature profiles assumed across interfacial gap

$$q_{\text{int}} = h_{gap}\left(T_s - T_{mold}\right) \quad [3.3]$$

$$h_{gap} = \cfrac{1}{\left(r_{contact} + \dfrac{d_{air}}{k_{air}} + \dfrac{d_{solid}}{k_{solid}}\right) + \left(\cfrac{1}{\dfrac{1}{\dfrac{d_{liquid}}{k_{liquid}} + \dfrac{d_{eff}}{k_{eff}}} + h_{rad}}\right)} \quad [3.4]$$

$$h_{rad} = \begin{cases} \cfrac{m^2\sigma(T_s^2 + T_{mold}^2)(T_s + T_{mold})}{0.75a(d_{liquid} + d_{eff}) + \dfrac{1}{e_{mold}} + \dfrac{1}{e_{steel}} - 1} & \left(T_{mprime} \geq T_{crystal}\right) \\[4ex] \cfrac{m^2\sigma(T_s^2 + T_{crystal}^2)(T_s + T_{crystal})}{0.75a(d_{liquid} + d_{eff}) + \dfrac{1}{e_{slag}} + \dfrac{1}{e_{steel}} - 1} & \left(T_{crystal} < T_{mprime}\right) \end{cases} \quad [3.5]$$

where

q_{int} = heat flux transferred across gap (Wm^{-2})

h_{gap} = effective heat transfer coefficient across the gap (Wm^{-2}K^{-1})

h_{rad} = radiation effective h (Wm^{-2}K^{-1})

T_s = surface temperature of the steel shell (°C)
T_{mprime} = mold temperature+mold/slag contact resistance delta T (°C)
T_{mold} = surface temperature of the mold (outermost coating layer) (°C)
$T_{crystal}$ = mold flux crystallization temperature (°C)
$r_{contact}$ = flux/mold contact resistance(m^2K/W)
d_{air}, d_{solid}, d_{liquid}, d_{eff} = thickness of the air gap, solid, liquid flux, and oscillation mark layers (mm)
k_{air}, k_{solid}, k_{liquid}, k_{eff} = conductivity of the air gap, solid, liquid flux, and oscillation mark layers (W/mK)
m = flux refractive index
σ = Stefan Boltzman constant (Wm^{-2}K^{-4})
a = flux absorption coefficient (m^{-1})

ε_s, ε_m = steel, mold surface emmisitivities

The calculation of some of the above variables is explained in the next section. Other variables are input data, defined in the Nomenclature section.

Fig **Error! Reference source not found.**.3 Thermal resistances used in the interface model

D. Heat Conduction in the Mold

Temperatures within the mold, including in particular the hot and cold face temperatures, are calculated knowing the heat fluxes, q_{cold} and q_{int}, and the effective heat transfer coefficient to the water, h_{water}.

Two dimensional, steady state temperature distribution within a rectangular section through the mold is calculated in the upper portion of the mold. It is found that the temperature is nearly linear in the mold thickness direction about 50 mm or so below the meniscus. Thus, a 1D assumption is adopted in the model below the distance zana below the meniscus.

Fig **Error! Reference source not found.**.4 Mold Temperature Calculation

16

E. Effective Heat Transfer Coefficient at Mold Cold Face:
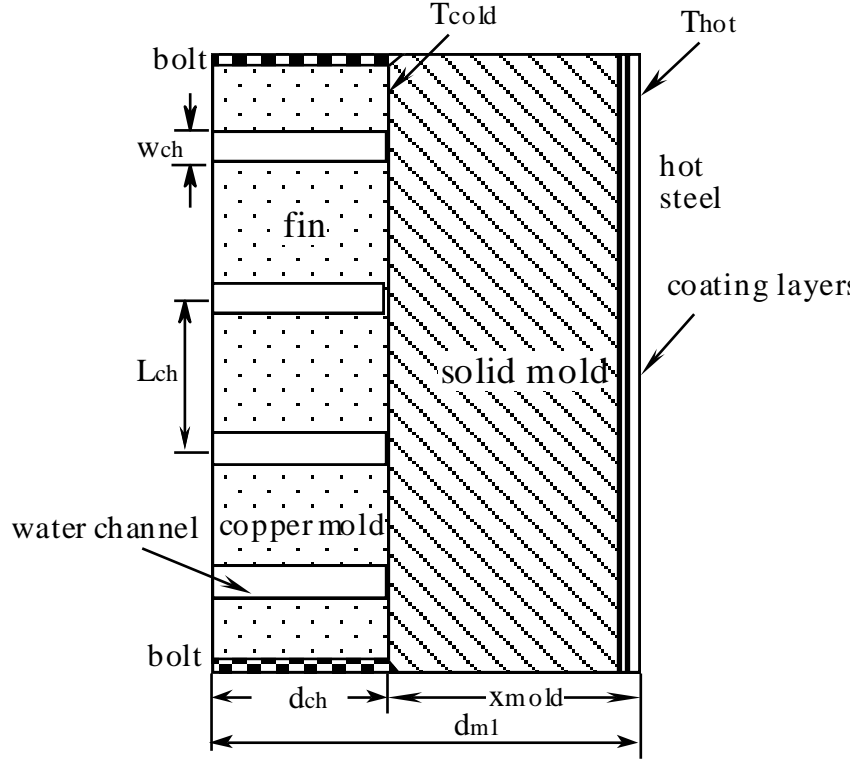
Fig **Error! Reference source not found.**.5 Water Channel in the mold

The effective heat transfer coefficient between the cooling water and the cold face ("water-side") of the mold copper, h_{water}, is calculated using the following formula, which includes a possible resistance due to scale build-up:

$$h_{water} = 1 \bigg/ \left(\frac{d_{scale}}{k_{scale}} + \frac{1}{h_{fin}} \right) \qquad [3.6]$$

To account for the complex nature of heat flow in the undiscretized width direction, the heat transfer coefficient between the mold cold face and cooling water, h_{fin}, is obtained using the following formula which treats the sides of the water channels as heat-transfer fins.

$$h_{fin} = \frac{h_w w_{ch}}{L_{ch}} + \frac{\sqrt{2 h_w k_{mold} \left(L_{ch} - w_{ch} \right)}}{L_{ch}} \tanh \sqrt{\frac{2 h_w d_{ch}^2}{k_{mold} \left(L_{ch} - w_{ch} \right)}} \qquad [3.7]$$

Where, L_{ch}, w_{ch}, d_{m1}, d_{ch} are geometry parameters shown in Fig **Error! Reference source not found.**.5 and k_m is the mold (copper) thermal conductivity. The presence of the water slots can either enhance or diminish the heat transfer relative to

a mold with constant thickness (equal to the minimum distance between the root of the water channel and the hot face). Deep, closely-spaced slots augment the heat transfer coefficient, (h_{fin} larger than h_w) while shallow, widely-spaced slots inhibit heat transfer. In most molds, h_{fin} and h_w are very close.

In Fig **Error! Reference source not found.**.5, the heat transfer coefficient between the water and the sides of the water channels, h_w, is calculated assuming turbulent flow through a pipe[25]:

$$h_w = \frac{k_{water}}{D}\left(5 + 0.015\,\mathrm{Re}_{waterf}^{c_1}\,\mathrm{Pr}_{waterw}^{c_2}\right) \qquad [3.8]$$

Here D is the equivalent diameter of the water channel, c_1 and c_2 are the empirical constants.

$$D = \frac{2w_{ch}d_{ch}}{w_{ch} + d_{ch}} \qquad [3.9]$$

$$c_1 = 0.88 - 0.24/\left(4 + \mathrm{Pr}_{waterw}\right) \qquad [3.10]$$

$$c_2 = 0.333 + 0.5e^{-0.6\mathrm{Pr}_{waterw}} \qquad [3.11]$$

$$\mathrm{Re}_f = \frac{\rho_{water}v_{water}D}{\mu_{waterf}} \qquad [3.12]$$

$$\mathrm{Pr}_w = \frac{\mu_{waterw}Cp_{water}}{k_{waterw}} \qquad [3.14]$$

The properties of the water, needed in the above equations, can be treated as either constants or temperature dependent variables evaluated at the film temperature (half-way between the water and mold wall temperature), according to the selection in the input data file made by the user.

F. 1D Steady State Temperature Model of Mold:

Hot face temperatures at or near the mold surface are calculated from the thickness of the copper, d_m, the water side heat transfer coefficient, and the interfacial heat flux, explained in a later section.

$$T_{hotc} = T_{water} + q_{int}\left(\frac{1}{h_{water}} + \frac{d_m}{k_m}\right)$$

[3.15a]

Further hot face temperatures are calculated by incorporating the resistances of the various thin coating layers, (Ni, Cr, air gap etc.), which vary with distance down the mold according to the input file:

$$T_{hot} = T_{water} + q_{int}\left(\frac{1}{h_{water}} + \frac{d_m}{k_m} + \frac{d_{ni}}{k_{ni}} + \frac{d_{cr}}{k_{cr}} + \frac{d_{poly}}{k_{poly}}\right)$$

[3.15b]

$$T_{mprime} = T_{water} + q_{int}\left(\frac{1}{h_{water}} + \frac{d_m}{k_m} + \frac{d_{ni}}{k_{ni}} + \frac{d_{cr}}{k_{cr}} + \frac{d_{poly}}{k_{poly}} + \frac{d_{air}}{k_{air}}\right)$$

[3.15c]

The hot face temperatures include the surface of the copper, T_{hotc}, the surface of the outermost mold plating layer, T_{hot} and the temperature at the interface between the air gap and the solid mold flux layer, T_{mprime}, including any contact resistance that might be present. The output file includes several temperatures:

$T_{hot} = (q + h_{mold1} * T_{water})/h_{mold1}$
$T_{hotc} = T_{hot} - dT_{coat}$
$T_{cold} = T_{hotc} - q * d_{mold}/tk_{mold}$

In these equations, the copper thickness, d_m, varies with distance down the mold, according to the mold curvature:

Outer radius:

$$d_{mold}^{outer} = d_{moldo}^{outer} + \sqrt{R_O^2 - \frac{1}{4}\left(Z_{mold\_total}\right)^2} - \sqrt{R_O^2 - \frac{1}{4}\left(Z_{mold\_total}\right)^2 - Z_{mold\_total}^2}$$

[3.16]

Inner radius

$$d_{mold}^{inner} = d_{moldo}^{inner} - \sqrt{R_I^2 - \frac{1}{4}\left(Z_{mold\_total}\right)^2} + \sqrt{R_I^2 - \frac{1}{4}\left(Z_{mold\_total}\right)^2 - Z_{mold\_total}^2}$$

[3.17]

where d_{moldo} is the mold thickness at the top of the mold, Z_{mold_total} is the total mold length (sum of working mold length Z_{mold} and distance of meniscus from top of the mold Z_{men}) and R_O, R_I are mold outer and inner radius of curvature respectively.

T_{cold} is the temperature of the root of the water channel, at the interface between the mold copper and the scale layer, if present:

$$T_{cold} = T_{water} + \frac{q_{int}}{h_{water}}$$

[3.18]

G. 2D Steady-State Temperature Model of Mold:

By assuming constant thermal conductivity in the upper mold and constant heat transfer coefficient between the mold cold face and the water channel along the casting direction, the two dimensional steady state heat conduction equation for mold temperature modification in meniscus region is the following Laplace equation:

$$\frac{\partial^2 T}{\partial x^2} + \frac{\partial^2 T}{\partial z^2} = 0$$

[3.19]

The actual hot face temperature of the mold is adjusted to account for the possible presence of mold coatings and air gaps:

$$T_{mold} = T\left(d_{mold}, z\right) + q_{int}\left(\frac{d_{ni}}{k_{ni}} + \frac{d_{cr}}{k_{cr}} + \frac{d_{poly}}{k_{poly}} + \frac{d_{air}}{k_{air}}\right)$$

[3.20]

H. Mold cooling water temperature rise:

A heat balance in the mold calculates the total heat extracted, q_{tin}, based on the increments of heat flux found in the interfacial heat flow calculation, q_{int} (W/m^2):

$$q_{tin} \text{ (kJ/m}^2\text{)} = \sum_{mold} q_{int} * \Delta t$$

[3.21]

The mean heat flux in the mold is calculated at the specified distance below the meniscus (usually at mold exit)

$$q_{ttot} \text{ (kW/m}^2\text{)} = \frac{q_{tin} V_c}{z}$$

[3.22]

The temperature rise of the cooling water is determined by:

20

$$\Delta T_{\text{cooling water}} = \sum_{\text{mold}} \frac{q_{\text{int}} \, V_c \, \Delta t \, L_{\text{ch}}}{\rho_{\text{water}} \, C_{\text{pwater}} \, V_{\text{water}} \, (\text{m/s}) \, w_{\text{ch}} \, d_{\text{ch}}}$$

[3.23]

This relation assumes that the cooling water slots have uniform dimensions, w_{ch} and d_{ch}, and spacing, L_{ch}. Heat entering the hot face (between two water channels) is assumed to pass entirely through the mold to heat the water flowing through the cooling channels. This calculation must be modified to account for missing slots due to bolts or water slots which are beyond the slab width, so do not participate in heat extraction. So the modified cooling water temperature rise is:

$$\Delta T_{\text{modified cooling water}} = \Delta T_{\text{cooling water}} * \frac{w_{ch} d_{ch}}{L_{ch}} * \frac{slab \quad width}{totcharea}$$

[3.24]

This cooling water temperature rise prediction is useful for calibration of the model with an operating caster.

I. Heat Transfer in the spray cooling zone:

Heat transfer in the spray cooling zones tracks the steel shell as it moves past each individual roll. Heat transfer is governed mainly by the spray heat transfer coefficient, which is calculated from the average spray water flow rate from the nozzle (Q_w) at each spray zone, using a general equation of the following form:

$$h_{\text{spray}} = A \cdot c \cdot Q_w^n \, (1 - b T_0)$$

[3.25]

Where, T_0 is water and ambient temperature in spray zone. In the model of Nozaki et al.[26], $A \cdot c = 0.3925$, $n = 0.55$, $b = 0.0075$.

Radiation is calculated based on radiation law. Heat extraction into the rolls should be considered.

J. Steel thermal properties (T_{liq}, T_{sol}, ρ, C_p, k and L_f):

T_{liq} and T_{sol}, are calculated by the program as a function of steel composition, based on the phase diagram for low-alloy steel. The properties, ρ, C_p, k and L_f can be treated in three ways. First, the carbon content and temperature dependent properties can be calculated based on the phase diagram for low carbon steel by the program. Alternatively, temperature dependent properties can be found from a set of empirical formula for stainless steel. Finally, ρ, C_p, k and L_f can be input as constants.

21

3.3. Abaqus Finite-Element Thermal Model

The model solves the transient heat-conduction equation [3.26] using commercial finite-element package Abaqus. Where H(T) and K(T) are the isotropic temperature-dependent enthalpy and conductivity, respectively.

$$\rho\frac{\partial H(T)}{\partial t} = \nabla \bullet (K(T)\nabla T) \qquad [3.26]$$

A 2-D simplification of the full 3-D process is reasonable, because axial (z direction) heat conduction is negligible relative to advection at the high Peclet number.

Along with boundary conditions:

Prescribed temperature on A_T

$$T = \hat{T}(\vec{X}, t) \qquad [3.26a]$$

Prescribed surface flux on A_q

$$(-k\nabla T) \bullet \vec{n} = \hat{q}(\vec{X}, t) \qquad [3.26b]$$

where ρ is density, k the isotropic temperature-dependent conductivity, H the temperature-dependent enthalpy, which includes the latent heat of solidification. $\hat{T}$ is a fixed temperature at the boundary A_T, $\hat{q}$ is the prescribed heat flux at the boundary A_q, which come from con1d calculating results, and $\vec{n}$ is the unit normal vector of the surface of the domain.

4. Stress Analysis

4.1. Governing Equations, Solutions Procedures

Inertial effects are negligible in solidification problems, so using the static mechanical equilibrium in Eq. 1 as the governing equation is appropriate

$$\nabla \cdot \boldsymbol{\sigma}(\mathbf{x}) + \mathbf{b} = 0 \tag{1}$$

where σ is the Cauchy stress tensor, and b is the body force density vector.

The rate representation of total strain in this elastic-viscoplastic model is given by Eq. (2):

$$\dot{\boldsymbol{\varepsilon}} = \dot{\boldsymbol{\varepsilon}}_{el} + \dot{\boldsymbol{\varepsilon}}_{ie} + \dot{\boldsymbol{\varepsilon}}_{th} \tag{2}$$

where $\dot{\boldsymbol{\varepsilon}}_{el}, \dot{\boldsymbol{\varepsilon}}_{ie}, \dot{\boldsymbol{\varepsilon}}_{th}$ are the elastic, inelastic, and thermal strain rate tensors respectively.

Viscoplastic strain includes both strain-rate independent plasticity and time dependant creep. Creep is significant at the high temperatures of the solidification processes and is indistinguishable from plastic strain. Kozlowski at al[27] proposed a unified formulation with the following functional form to define inelastic strain.

$$\dot{\varepsilon}\,(1/\sec.) = f\,(\%C)\left[\sigma\,(MPa) - f_1\left(T\left({}^oK\right)\right)\varepsilon|\varepsilon|^{f_2\left(T\left({}^oK\right)\right)-1}\right]^{f_3\left(T\left({}^oK\right)\right)} \exp\left(-4.465\times10^4\left({}^oK\right)\big/T\left({}^oK\right)\right)$$

$$f_1\left(T\left({}^oK\right)\right) = 130.5 - 5.128\times10^{-3}T\left({}^oK\right)$$

$$f_2\left(T\left({}^oK\right)\right) = -0.6289 + 1.114\times10^{-3}T\left({}^oK\right)$$

$$f_3\left(T\left({}^oK\right)\right) = 8.132 - 1.54\times10^{-3}T\left({}^oK\right)$$

$$f\,(\%C) = 4.655\times10^4 + 7.14\times10^4\%C + 1.2\times10^5\left(\%C\right)^2$$

$$\tag{5}$$

f_1, f_2, f_3, f_C are empirical temperature, and steel-grade-dependant constants. Another constitutive law, the modified power-constitutive model developed by Zhu[28], is used to simulate the delta-ferrite phase, which exhibits significantly higher creep rates and lower strength than the austenite phase.

The system of ordinary differential equations defined at each material point by the viscoplastic model equations is converted into two "integrated" scalar equations by the backward-Euler method and then solved using a special bounded Newton-Raphson method [29]in user subroutine UMAT.

Abaqus main code is using the fully implicit staggered coupled algorithm for time integration of the governing equations[30]. In each time step the thermal field is

solved, and then the resulting thermal strains are used to solve the mechanical problem. Newton-Raphson iteration continues until tolerances for both equation systems are satisfied before proceeding to the next time step.

4.2. A single layer of 3-D elements model

The domain adopted for this problem is a single layer of 3-D elements through the bloom thickness goes down in the axial z direction (the casting direction) with zero relative rotation. The x direction is thickness and y is width direction. In continuous casting process, one dimension of the casting is much longer than the others, and otherwise unconstrained. It is reasonable to apply a condition of generalized plane strain on down face in the long direction (z) and fixed upper face. The strain in z direction does not vary with x-y coordinates. For the nodes in other faces, the displacements can be dealt with as Fig **Error! Reference source not found.**.1
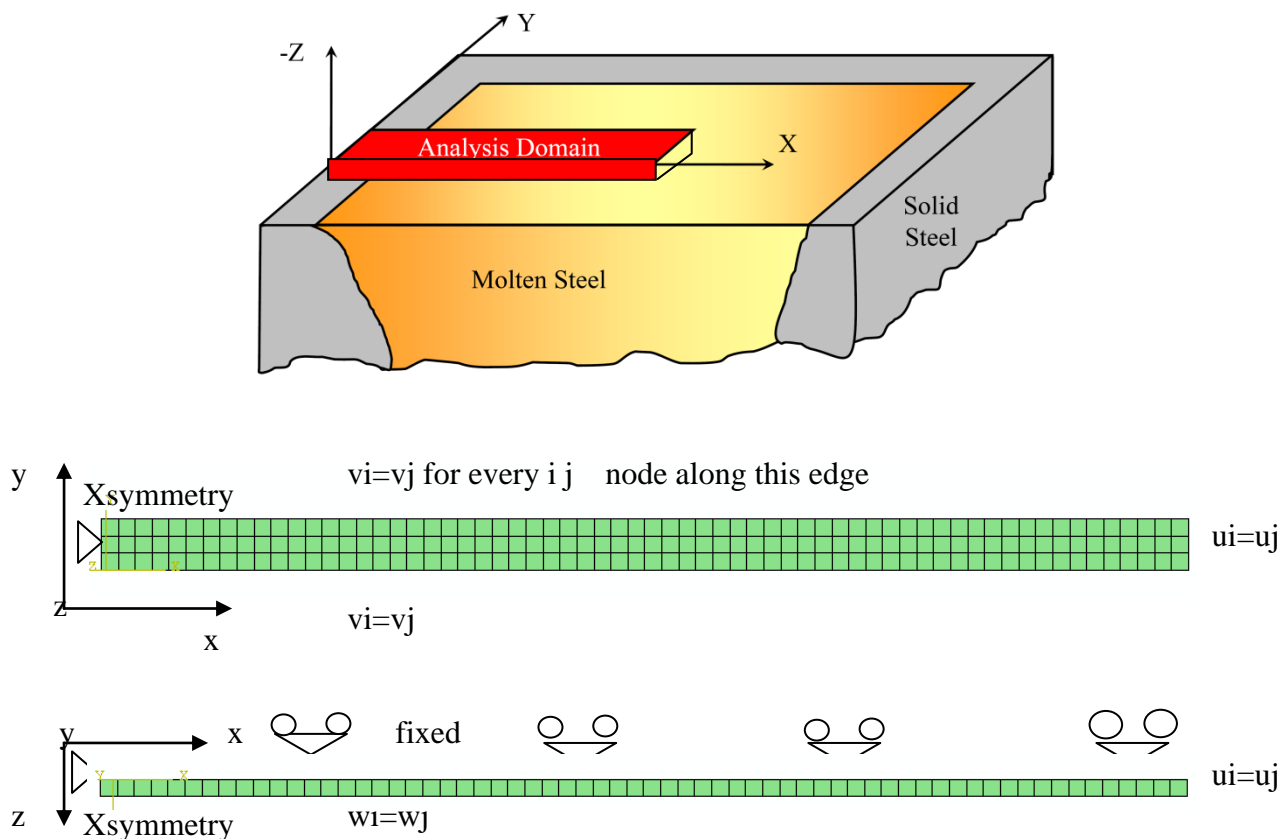
Fig **Error! Reference source not found.**.1 Mechanical FE domains of 3D single layer model

The other boundary condition include: Buldging can be set by displacement; at bending and unbending sections, the angle should be set by 'equation' .

4.3. 2-D slice model

The domain adopted for this problem is a quarter of thin slice goes down in the axial z direction (the casting direction). Y axial is thickness direction and x axial is width direction. The generalized plane strain elements can be used in the axial of z direction with zero relative rotation (i.e. $\varepsilon_{zz} = const$). Taking rolling effect into account, every node on wide side has same displacement in y direction and same displacement in x direction on narrow side as following Fig **Error! Reference source not found.**.2. The displacement of width wide depends on openness of rollers in y axial and bulging calculated from empirical equation; the displacement of narrow side depends on openness of rollers in x direction. It is difficult to take corner effect into account.
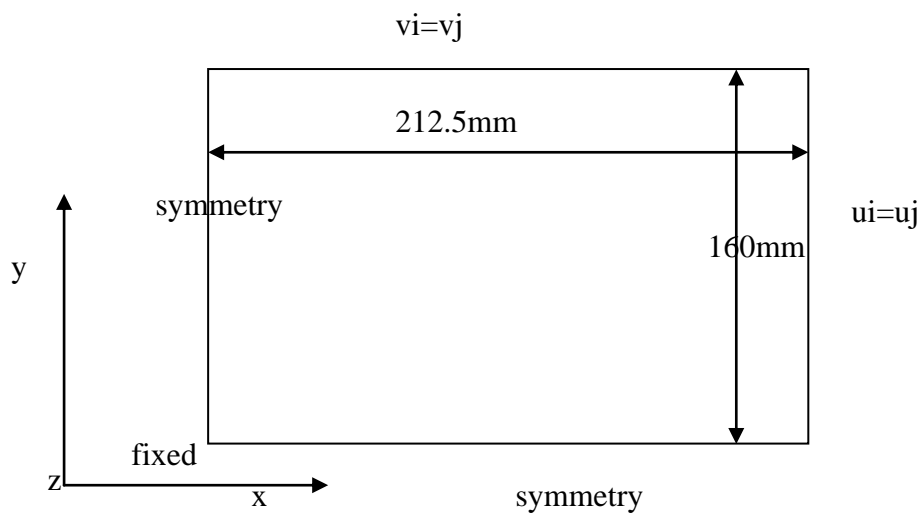
Fig **Error! Reference source not found.**.2 Mechanical domains of 2D model

5. Model Verification

5.1. Con1d model

The internal consistency and accuracy of various components of models have been verified through extensive comparison with analytical solutions. The accuracy of the 2-D mold heat-transfer model at the meniscus region was evaluated by comparison with full 3-D finite-element model computations on separate occasions using Abaqus[31] and with an in-house code.[32] In both cases, the Con1d model predictions matched within the uncertainties associated with mesh refinement of the 3-D model. Other obvious checks include ensuring that the temperature predictions match at the transition between at 2-D and 1-D regions, which also indicates when heat flow is 1-D.

The Con1d solidification model is verified here through comparison with an analytical solution for 1-D heat conduction with phase change.[33,34] This solution assumes a constant shell-surface temperature and constant steel properties. Table **Error! Reference source not found.**.1 lists the constants used in both the analytical solution and the Con1d validation case, which are chosen for typical conditions expected in practice. The difference between the steel liquidus and solidus temperatures is only 0.1 C to approximate the single melting temperature assumed in analytical solution, which is set to the mean of T_{liq} and T_{sol} used in Con1d. The pour temperature is set to the liquidus because the superheat is neglected in the analytical solution. For the Con1d model, the time-step size Δt is 0.004 seconds and the node spacing is 0.5 mm.

Fig **Error! Reference source not found.**.1 compares results from the analytical solution and Con1d model for (a) the temperature distribution through the shell at different times and (b) the growth of the shell thickness with time. The results show that the predictions of the Con1d model are very accurate, so the same time step and mesh are used in the following cases.

Table **Error! Reference source not found.**.1 Constants used in analytical solution and validation case

Conductivity, k_{steel}	30	W/mK
Specific Heat, Cp_{steel}	670	J/kgK
Latent Heat, L_f	271	kJ/kg
Density, ρ_{steel}	7400	Kg/m^3

Melting Temperature, T_{melt}	1509.05	C
Liquidus Temperature, T_{liq}	1509.1	C
Solidus Temperature, T_{sol}	1509	C
Shell Surface Temperature, T_s	1000	C
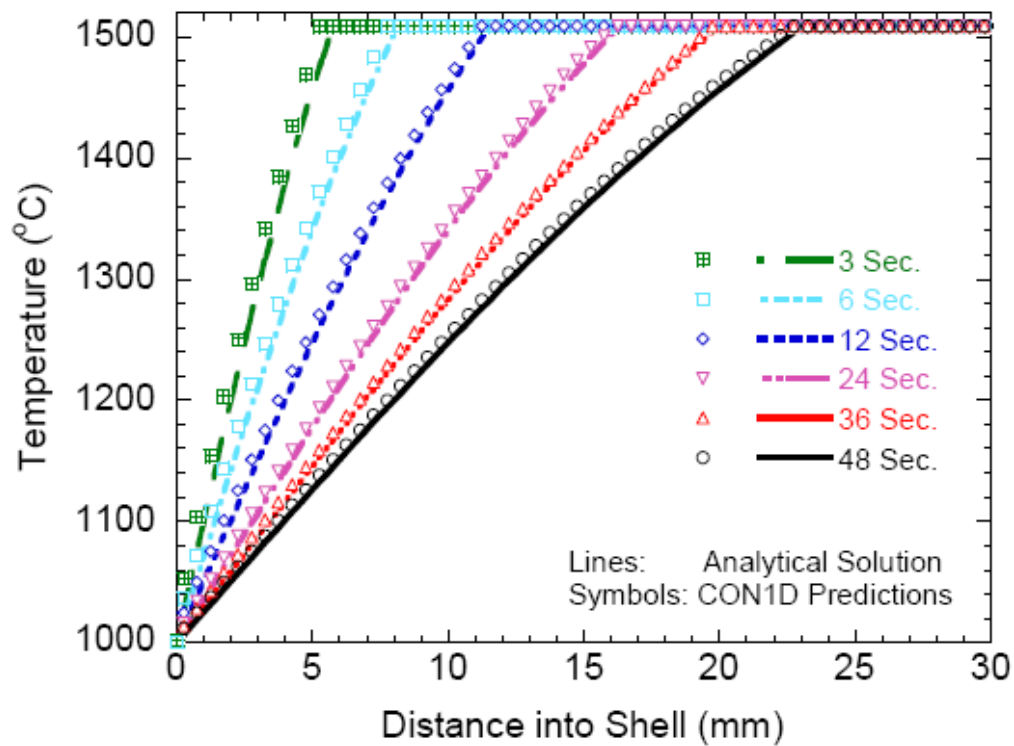
(a) Shell temperature distribution
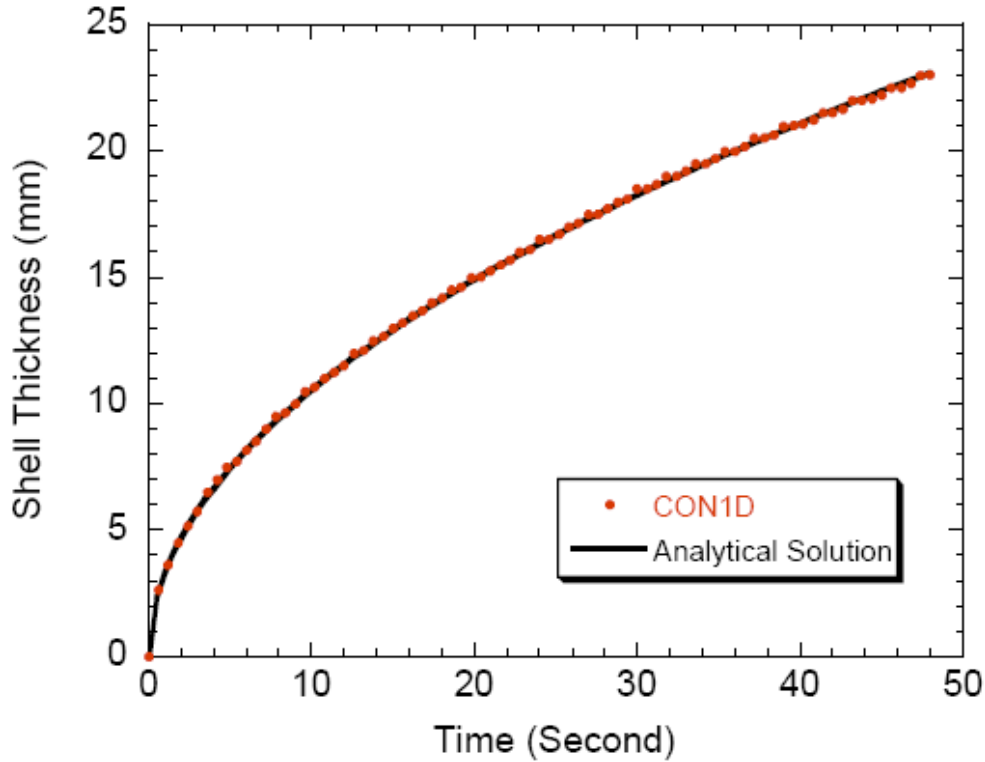
(b) Shell growth

Fig **Error! Reference source not found.**.1 Comparison of Con1d model results and analytical solution.

5.2. Abaqus model

A semi-analytical solution of thermal model in an unconstrained solidifying plate, derived by Weiner and Boley[35] is used here as an ideal validation problem for solidification model. This 1D solution takes advantage of the large length and width of the casting. Thus, it is reasonable to apply the generalized plane strain condition, in both the y and z directions, to produce the complete 3-D stress and strain state.

The domain adopted for this problem is a thin slice through the plate thickness using 2-D generalized plane strain elements (in the axial z direction) with zero relative rotation. The domain moves with the strand in a Langrangian frame of reference as shown in Fig **Error! Reference source not found.**.2. In addition, a second generalized plane strain condition was imposed in the y direction (parallel to the surface) by coupling the displacements of all nodes along the bottom edge of the slice domain as shown in Fig **Error! Reference source not found.**.3. This was accomplished using the *EQUATION option in abaqus. The normal (x) displacement of all nodes along the bottom edge of the domain is fixed to zero. Tangential stress was left equal zero along all surfaces. Finally, the ends of the domain are constrained to remain vertical, which prevents any bending in the xy plane.
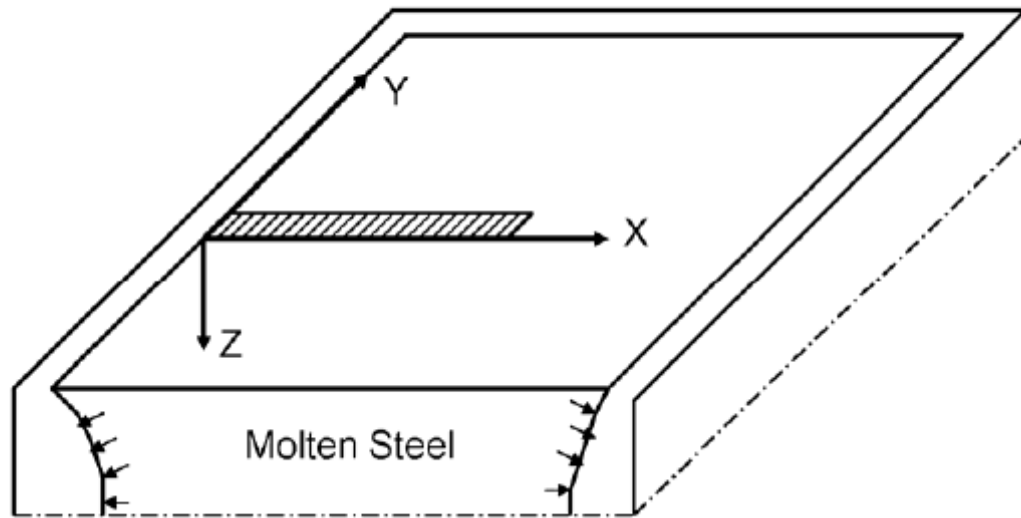
Fig **Error! Reference source not found.**.2 Solidifying slice.

The material in this problem has elastic-perfectly plastic constitutive behavior. The yield stress drops linearly with temperature from 20 Mpa at 1000 C to zero at the solidus temperature 1494.4 C, which was approximated by 0.03 Mpa at the solidus temperature. A very narrow mushy region, 0.1 C, is used to approximate the single melting temperature assumed by Boley and Weiner. All the constants used in this solidification model are listed in Table l.

Table **Error! Reference source not found.**.2 Constants used in solidification test problem.

Conductivity (W/mK)	33.0
Specific heat (J/kgK)	661.0
Elastic modulus in solid (Gpa)	40.0
Elastic modulus in liquid (Gpa)	14.0
Thermal linear expansion coefficient (1/K)	0.00002
Density (kg/m^3)	7500.0
Posisson's ratio	0.3
Liquidus temperature (C)	1494.45
Fusion temperature (analytical) (C)	1494.4

Solidus temperature (C)	1494.35
Initial temperature (C)	1495.0
Latent heat (J/kg K)	272000.0
Reciprocal of liquid viscosity (MPa^{-1}s^{-1})	1.5×10^8
Surface film coefficient (W/m^{2}K)	250000
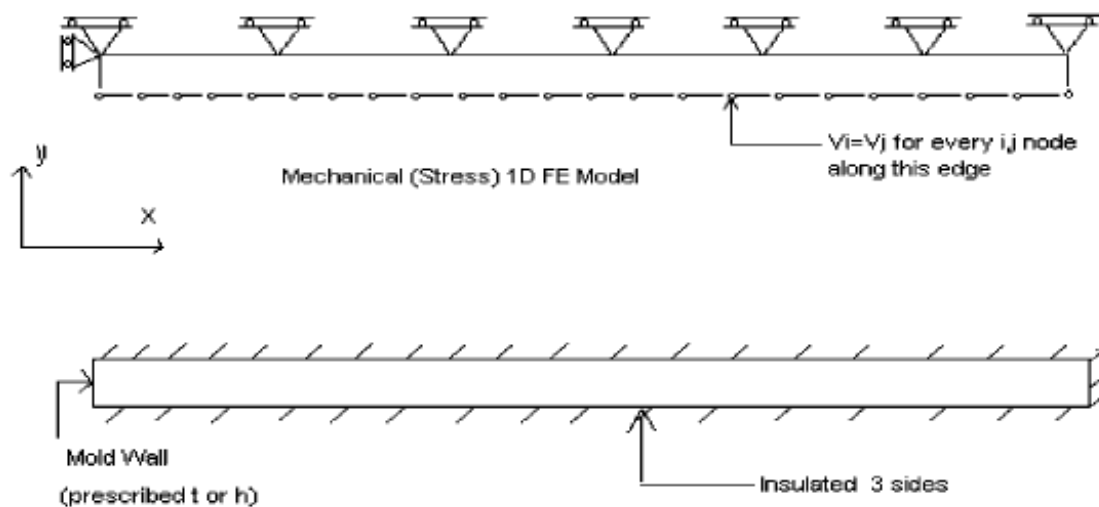
Fig **Error! Reference source not found.**.3 Mechanical and thermal FE domains.

Fig Error**! Reference source not found.**.3 shows the domain and boundary conditions for both the heat transfer and mechanical models. Heat transfer analysis is run first to get the temporal and spatial temperature field. Stress analysis is then run using this temperature field. The domain in Abaqus has a single row of 300 plane four-node elements in both thermal and stress analysis. Con2d uses a similarly refined mesh with six-node, quadratic triangular elements.[36]

Fig Error**! Reference source not found.**.4 and Fig **Error! Reference source not found.**.5 show the temperature and the stress distribution across the solidifying shell at two different solidification times. The semi-analytical solutions were computed with MATLAB by Li and Thomas. The almost-linear temperature gradient through the shell gradually drops as solidification proceeds. This faster cooling of the interior relative to the surface region naturally causes interior contraction and tensile stress, which is offset by compression at the surface. The changes in slope at ~-15 and +12 MPa denote the transition from the elastic central region to plastically yielded surface and interior. Both lateral stress distributions (y and z directions) are the same for both codes, which is expected from the identical boundary conditions in these two directions. Shear stresses and x-stress are all zero. Identical results were found with the perfectly plastic and the viscoplastic liquid functions coded in UMAT, so there is a

30

single Abaqus curve representation on the graphs. CON2D produced similar accuracy with the semi-analytical solution.
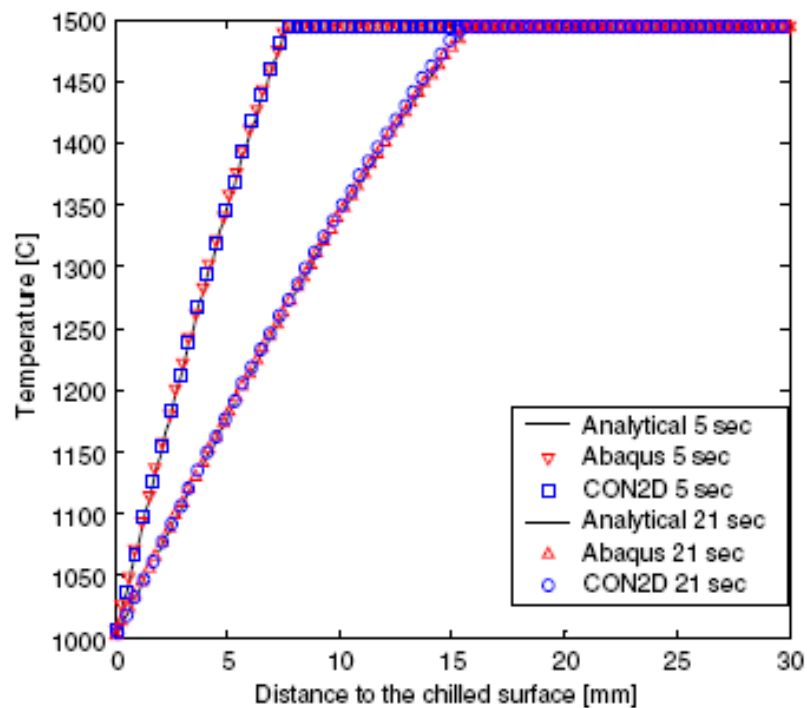
Fig **Error! Reference source not found.**.4 Temperature distribution along the solidifying slice.
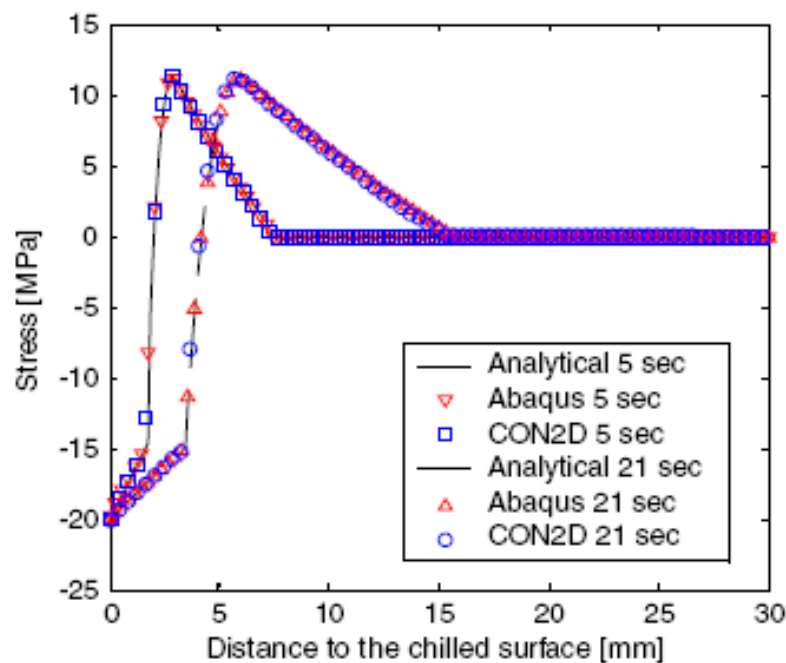
Fig **Error! Reference source not found.**.5 Y and Z stress distributions along the solidifying slice

6. Model Applications

6.1. Steel properties

Table **Error! Reference source not found.**.1 shows the steel grade composition and solidification properties.

Fig **Error! Reference source not found.**.1 contains the Fe-C phase diagram for C10, T91, T92, T23 and T122 calculated by Thermal-Calc. Fig **Error! Reference source not found.**.2 shows phase fraction variation with temperature. The alloy elements have a little influence on liquidus, but decrease solidus remarkably, which increases the temperature range of the mushy zone. There is a large ferrite phase zone during solidification. These high alloy steels are susceptible to segregation and cracks.

Table **Error! Reference source not found.**.1 steel grade component and solidification properties

Steel grade	C	Si	Mn	Cr	Mo	W	Liquidus	Solidus
T91	0.095	0.3	0.4	8.3	0.95	0	1512	1461
T92	0.115	0.4	0.45	8.7	0.4	1.65	1510	1441
C10	0.1						1526	1493
T122	0.115	0.4	0.45	11.5	0.4	2	1500	1431
T23	0.06	0.23	0.35	2.2	0.1	1.6	1528	1495
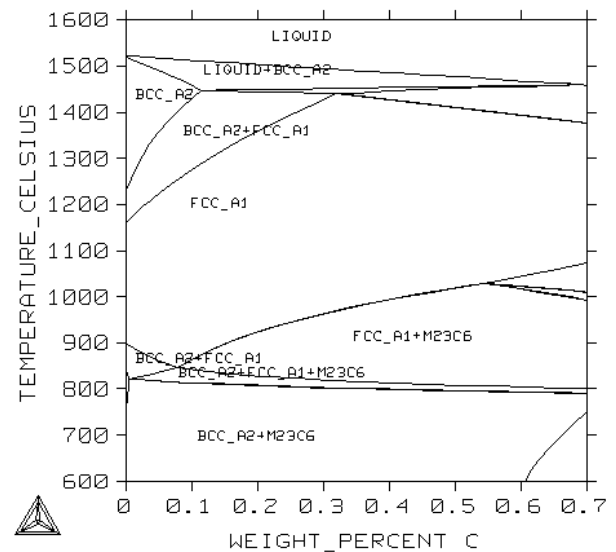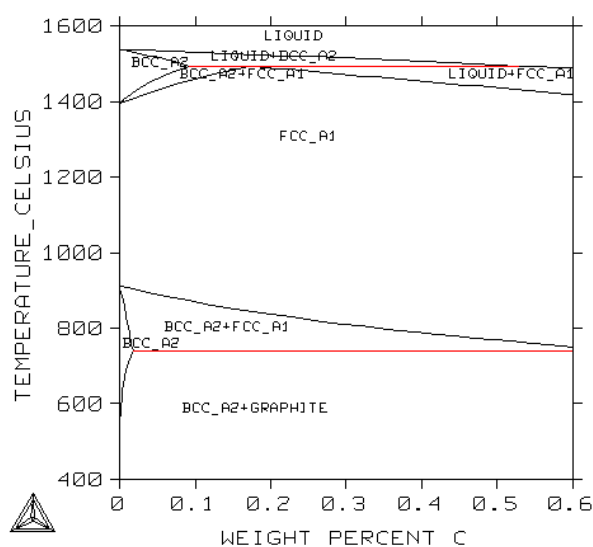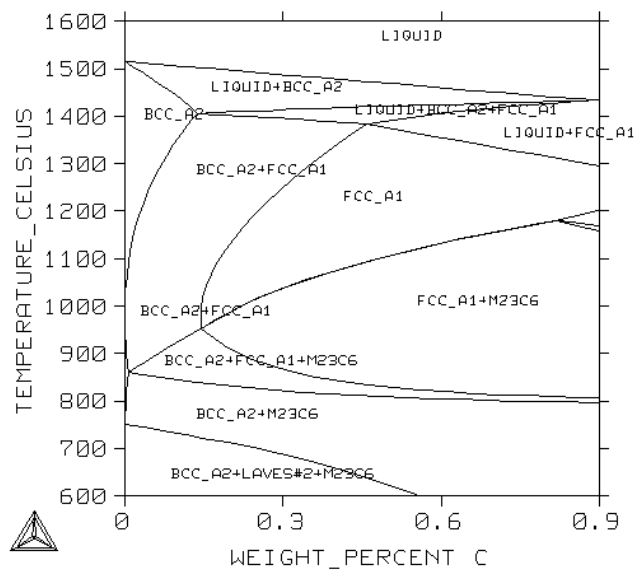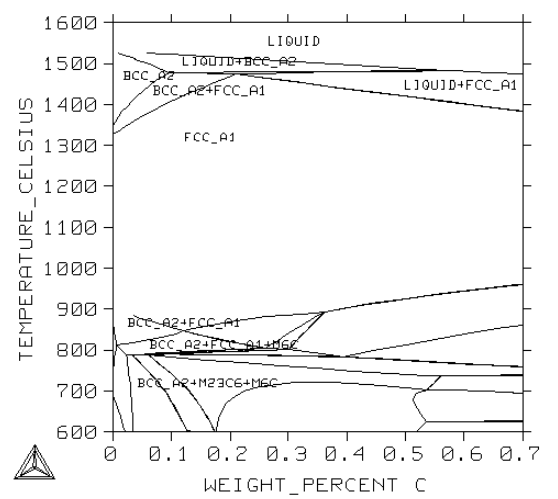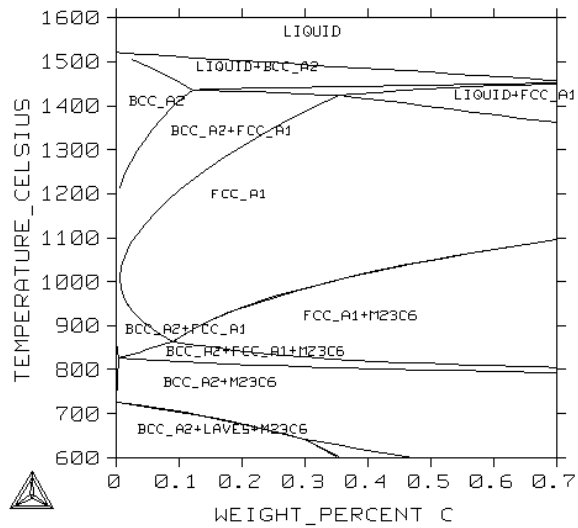
Fig **Error! Reference source not found.**.1 Fe-C phase diagram for C10, T91,T92,T23 and T122

Steel Phase Fraction (CON1D: t91)

180. 1.09478

Steel Phase Fraction (CON1D: t92)

3.933. 0.792701
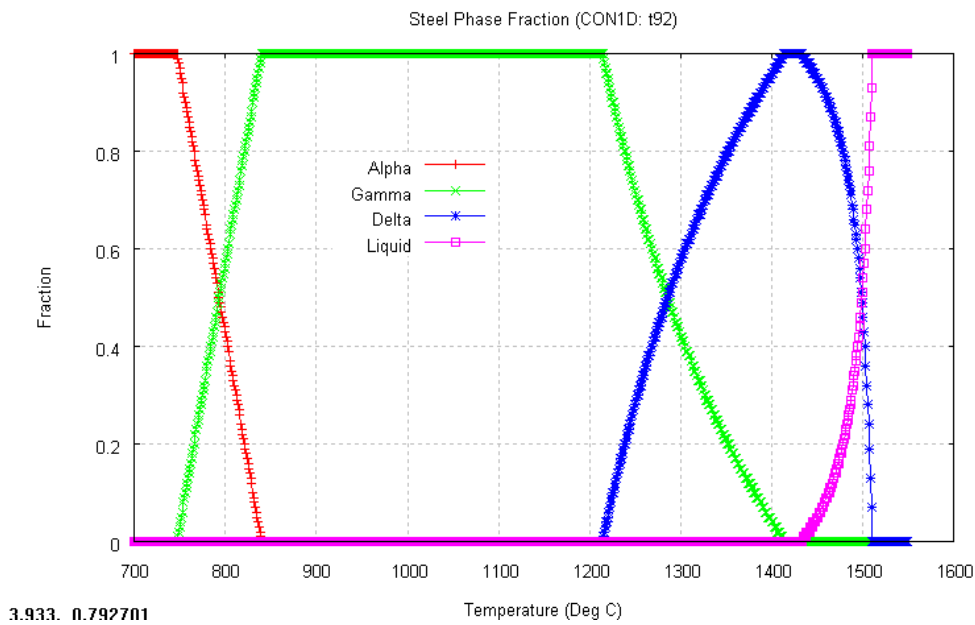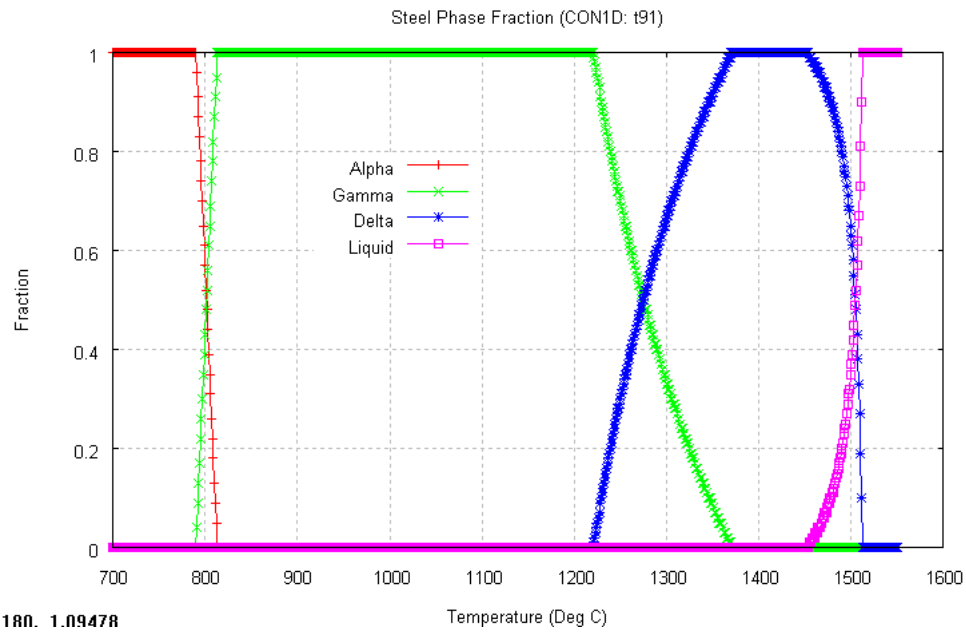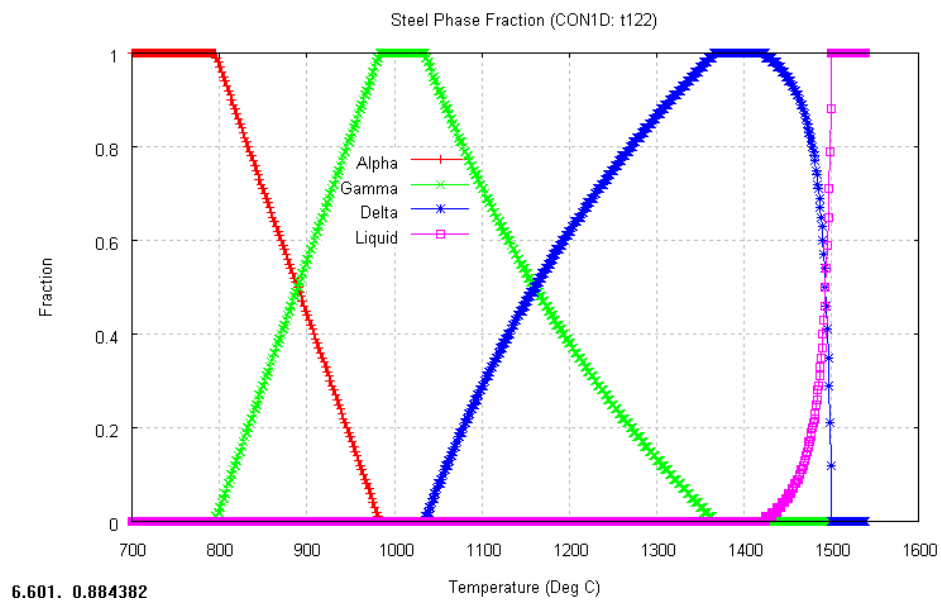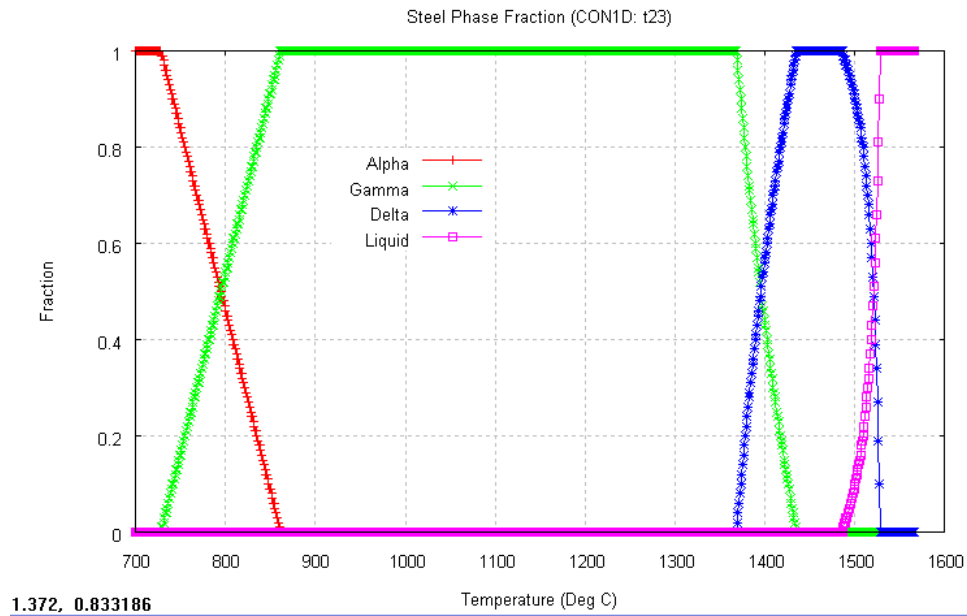
Fig **Error! Reference source not found.**.2 Phase fraction variation with temperature

The thermal conductivity of steel grades is measured by Baosteel and calculated as a function of temperature as given in Fig 6.3. The thermal conductivity of the liquid is not artificially increased, as is common in other models, because the effect of liquid

convection is accounted for in the superheat-flux function, which is calculated by the CON1D model, which includes the effects of turbulent flow in the mold. T91, T92 have the similar phases as ferrite stainless steel 410, we use the conductivity of 410 as T91 and T92's conductivity.
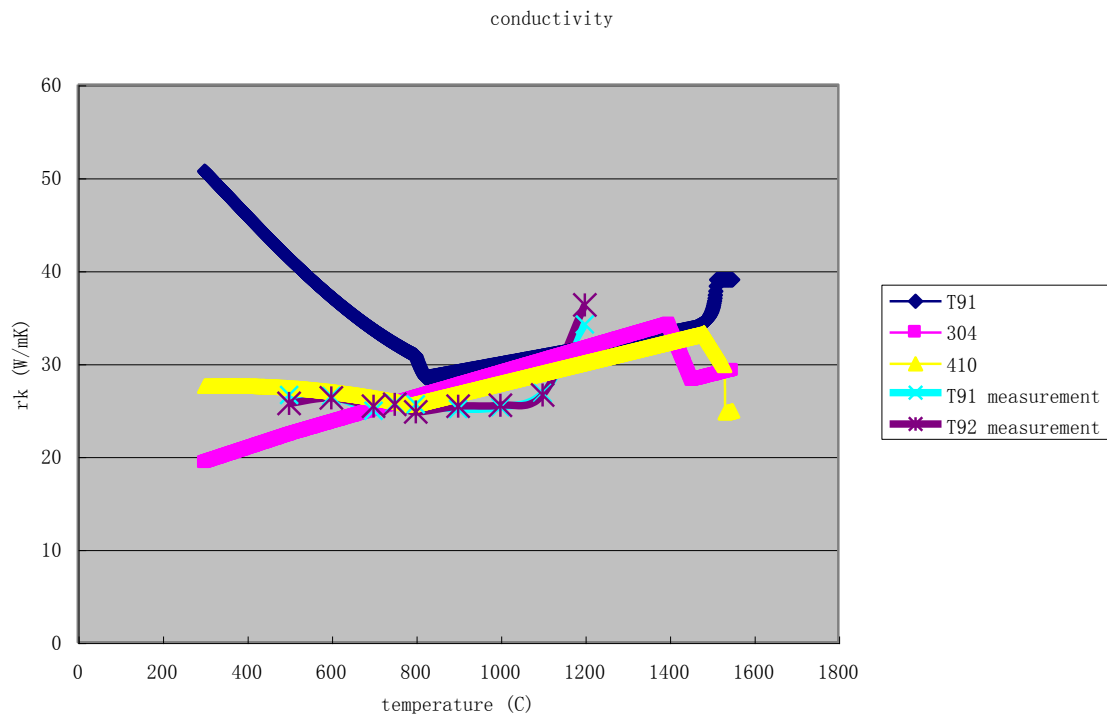
Fig **Error! Reference source not found.**.3   Comparison of model thermal conductivities and measurements

Fig **Error! Reference source not found.**.4 shows model specific heat and measurements of T91 and T92, which match well with each other.
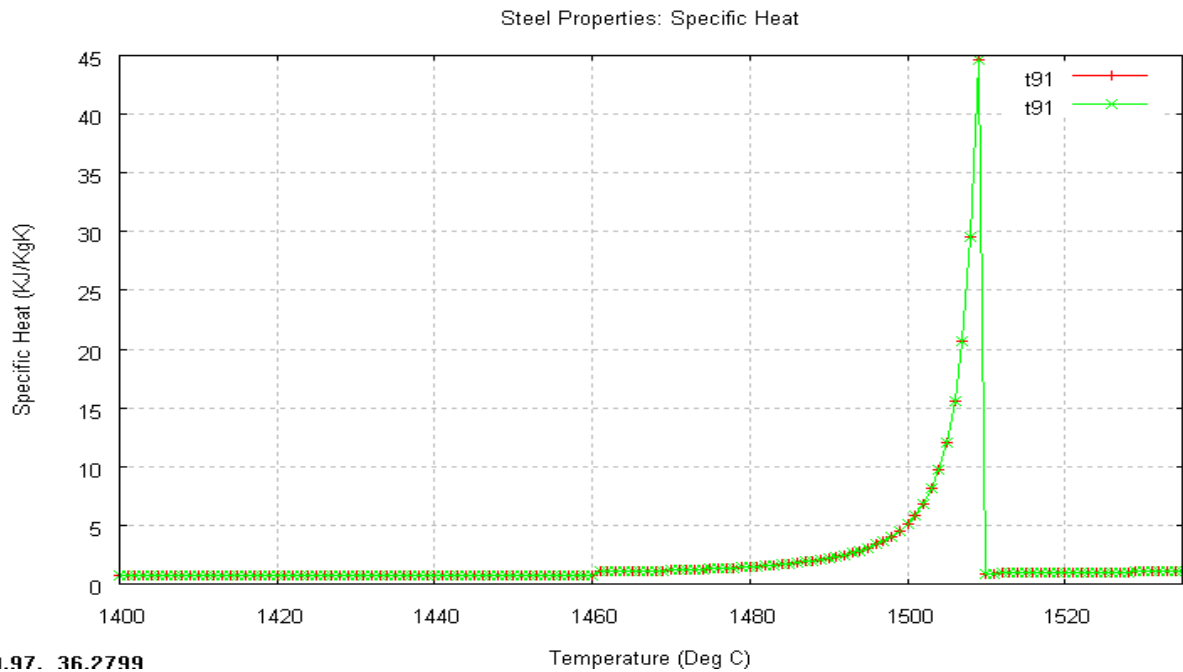
1.97, 36.2799
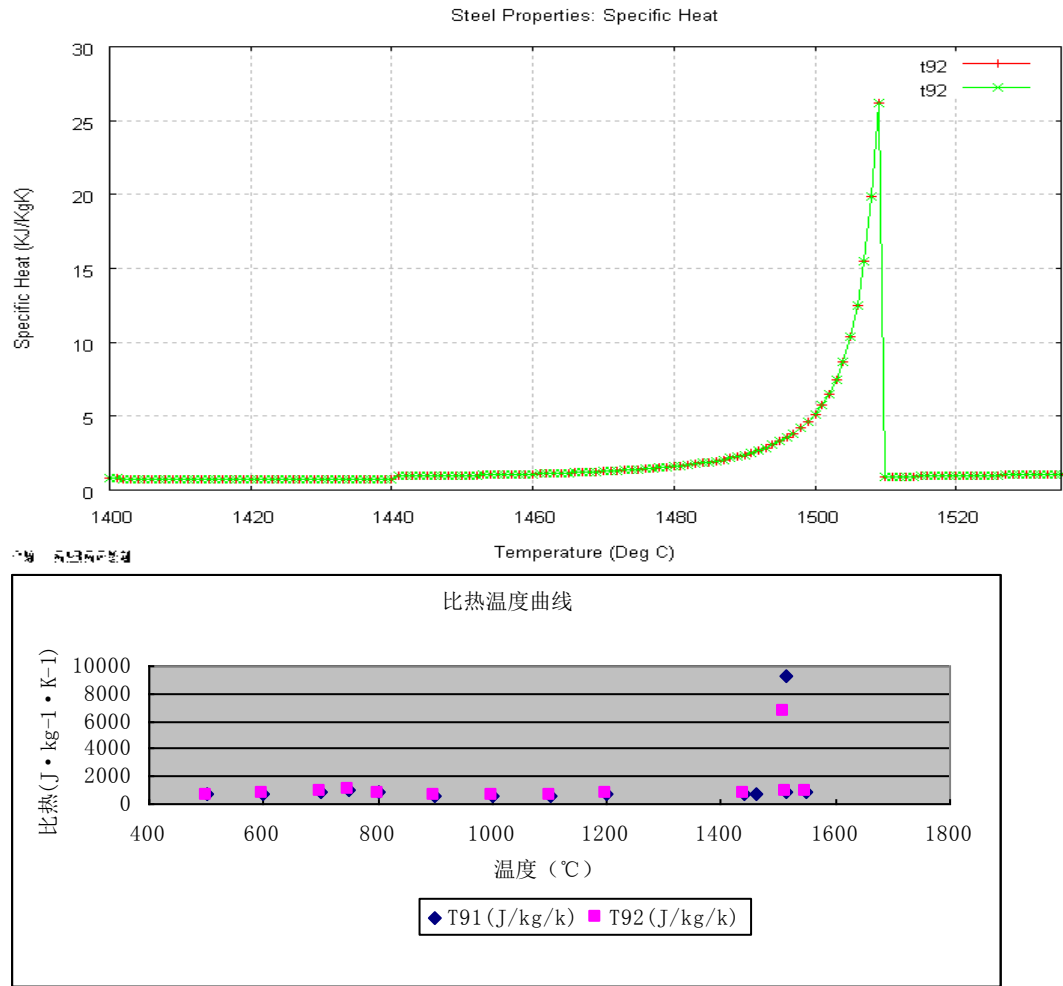
Fig **Error! Reference source not found.**.4 Model specific heat and measurements of T91 and T92

The results of thermal linear expansion of steel are calculated as composition and temperature-dependent function as following[37,38].

$$\text{TLE} = \sqrt[3]{\frac{\rho(T_0)}{\rho(T)}} - 1$$

$$\rho(\text{Kg/m}^3) = \rho_\alpha f_\alpha + \rho_\gamma f_\gamma + \rho_\delta f_\delta + \rho_l f_l$$

$$\rho_\alpha = 7881 - 0.324 T(°C) - 3 \times 10^{-5} T(°C)^2$$

$$\rho_\gamma = \frac{100(8106 - 0.51 T(°C))}{(100 - (\text{pct C}))(1 + 0.008(\text{pct C}))^3}$$

$$\rho_\delta = \frac{100(8011 - 0.47 T(°C))}{(100 - (\text{pct C}))(1 + 0.013(\text{pct C}))^3}$$

$$\rho_l = 7100 - 73(\text{pct C}) - (0.8 - 0.09(\text{pct C}))$$
$$(T(°C) - 1550)$$
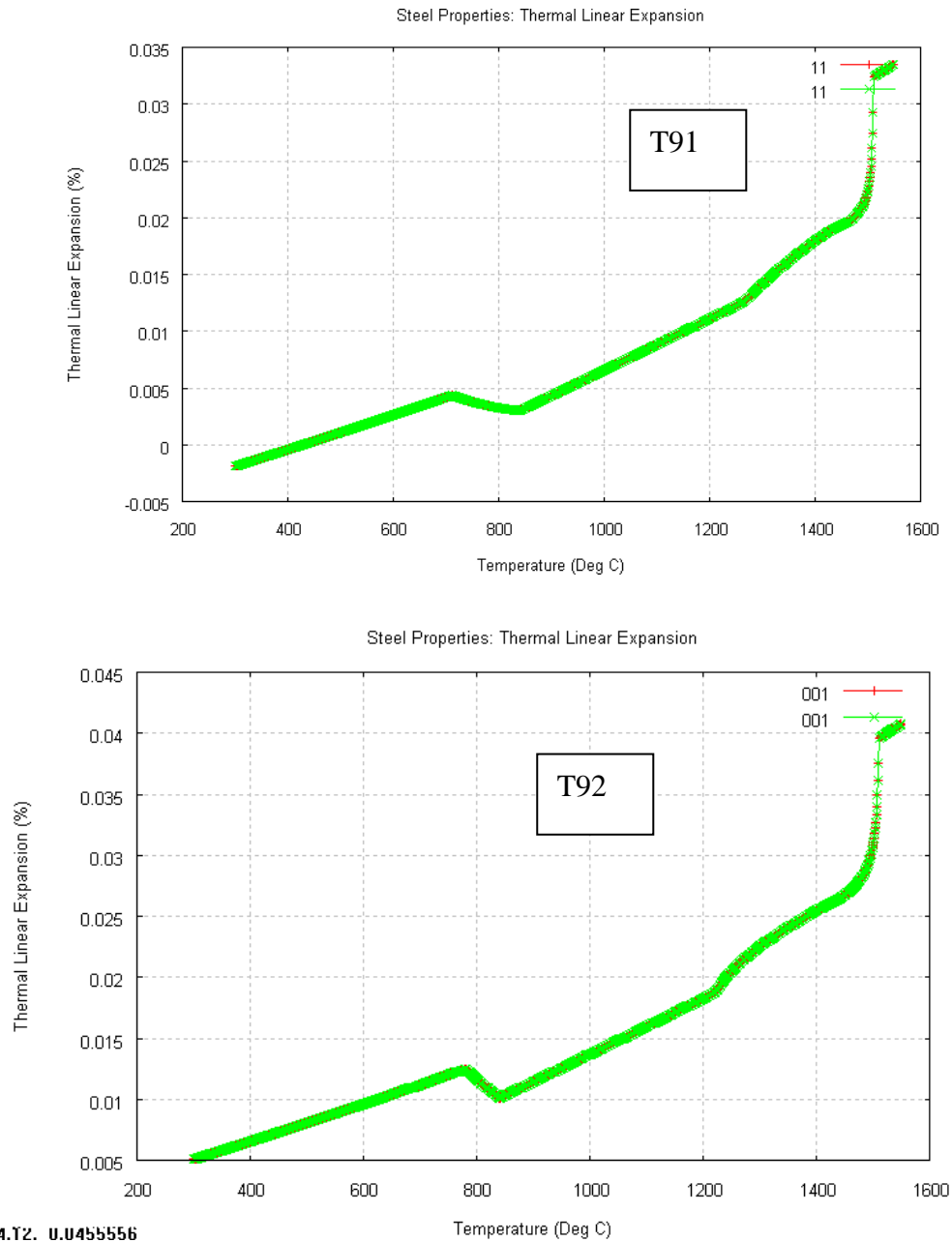
Fig **Error! Reference source not found.**.5 thermal linear expansion of steel are calculated as composition and temperature-dependent function

From phase fraction diagram and thermal linear expansion of steel, we can conclude that with increasing alloy composition for these steel grade, solidus decreases, mushy zone and ferrite phase zone become bigger, thermal linear expansion increase, then crack sensibility increases.

6.2. Simulation and measurement results

6.2.1 T91 steel

The T91 steel has been casted in Baosteel with 1550 C pour temperature and 0.6 m/min casting speed. Soft reduction for 1st strand is 8mm. The casting details are shown in T91 process specification. Fig **Error! Reference source not found.**.6 and Fig **Error! Reference source not found.**.7 show the heatflux of mold and film coefficient for calculation.
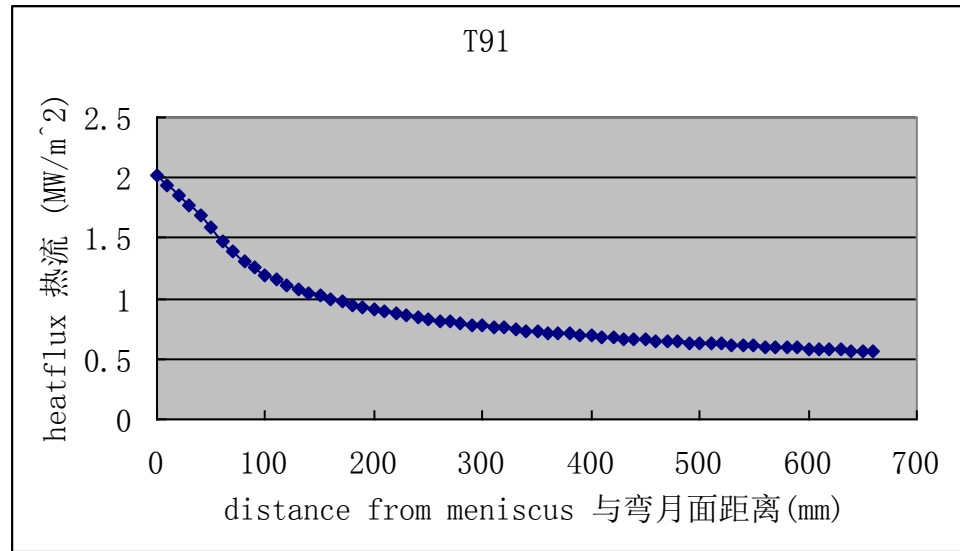
Fig **Error! Reference source not found.**.6 Heatflux of mold used in con1d and abaqus
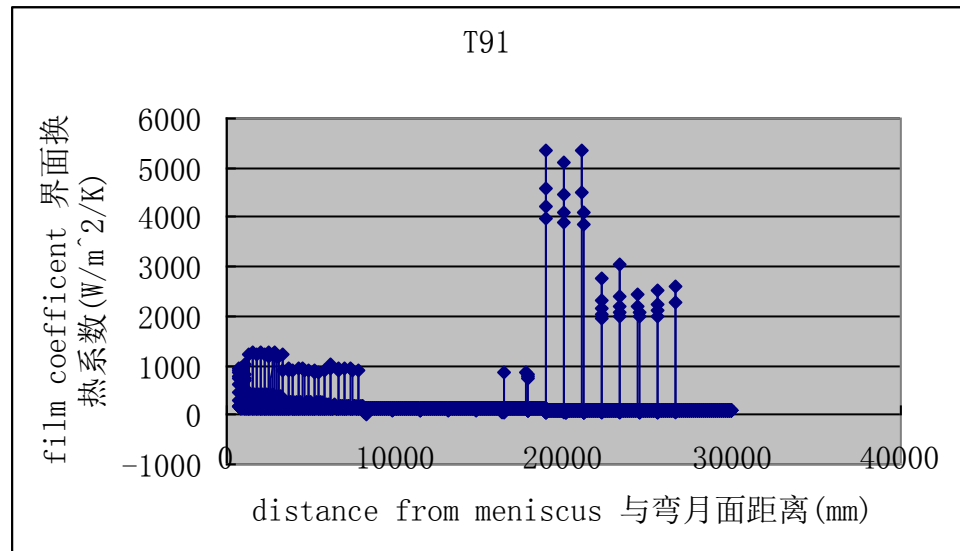
Fig **Error! Reference source not found.**.7 Film coefficient on strand surface

Fig **Error! Reference source not found.**.8 and Fig **Error! Reference source not found.**.9 show the thermal simulation results by con1d, Abaqus and measurement results. They match well.
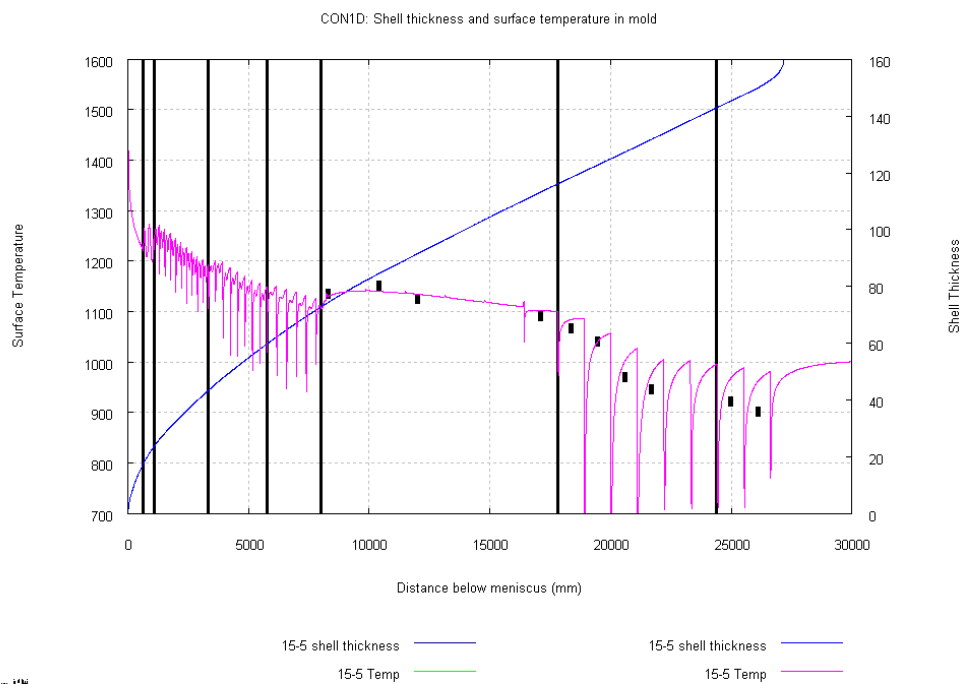
Fig **Error! Reference source not found.**.8 shell thickness and surface temperature in con1d and measurement
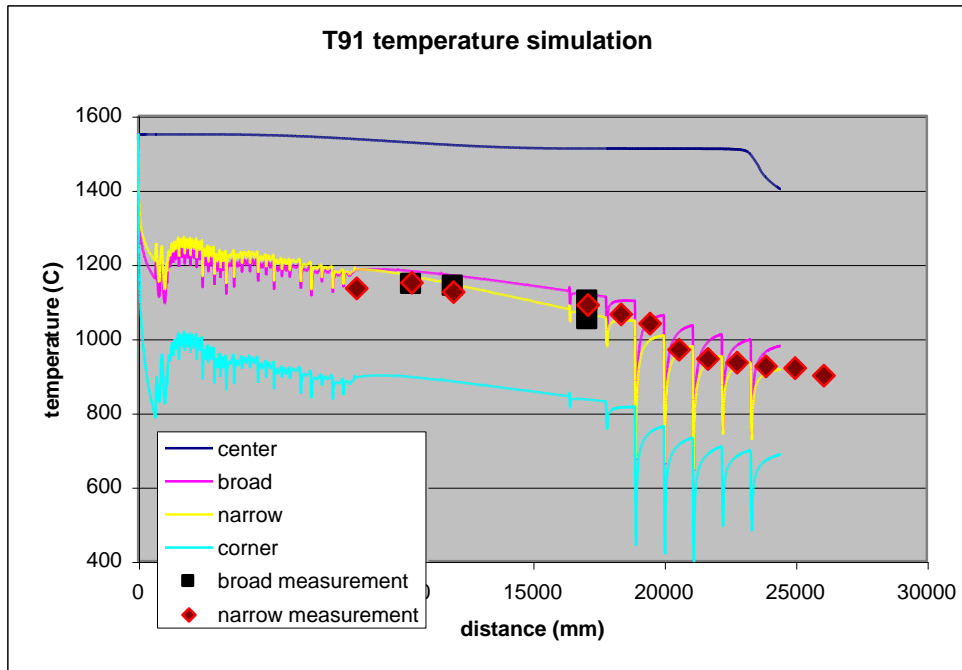
Fig **Error! Reference source not found.**.9 Temperature simulation by Abaqus and measurement.

Solid fraction, temperature distribution and temperature evolution of T91 is listed as following:
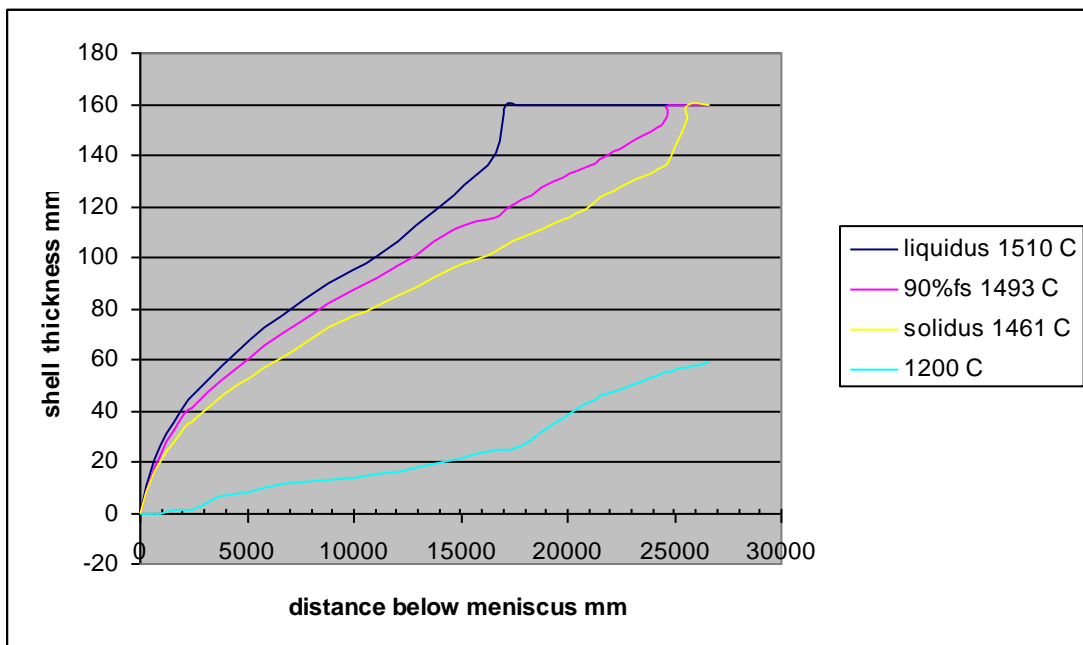
Fig **Error! Reference source not found.**.10 solid fraction of T91 by Abaqus
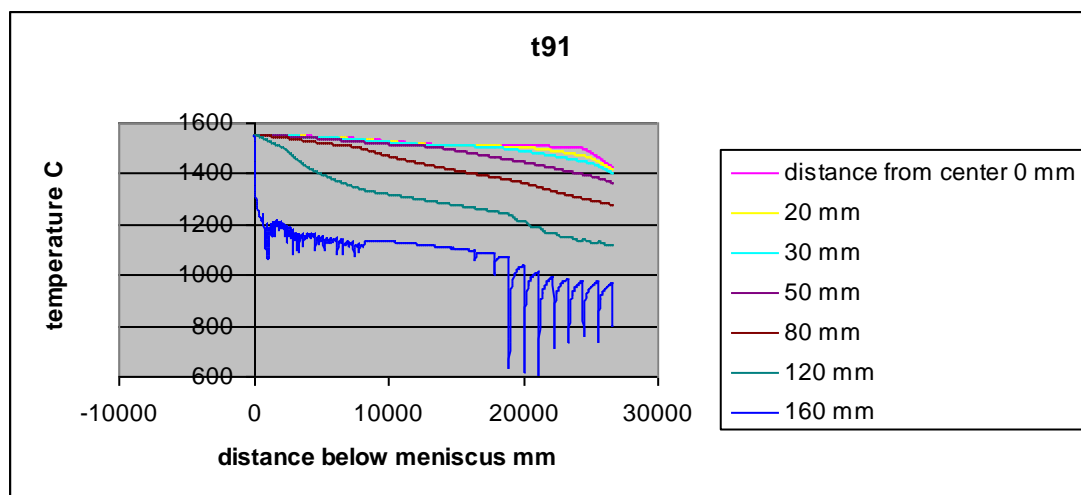
Fig **Error! Reference source not found.**.11 at different shell thickness, the temperature distribution of T91 by Abaqus
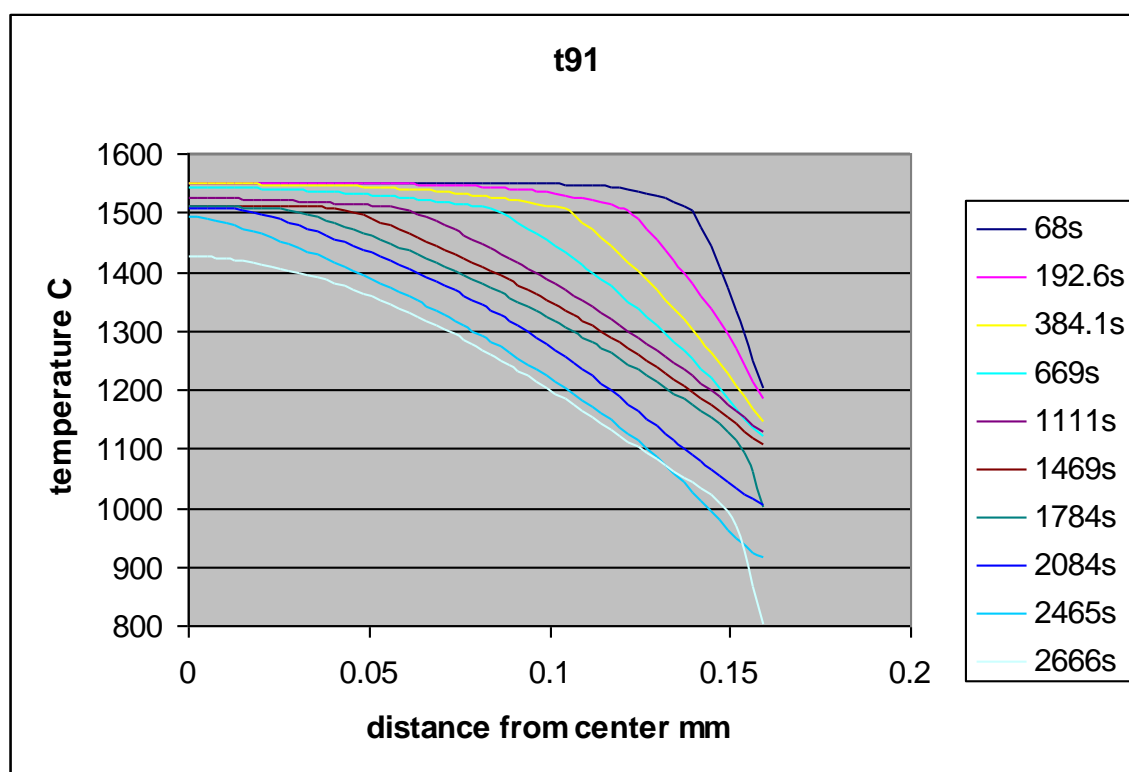
Fig **Error! Reference source not found.**.12 temperature evolution of T91 by Abaqus

Fig **Error! Reference source not found.**.13 shows Buldging results from empirical equations. We choose Lan equation results in our stress model.
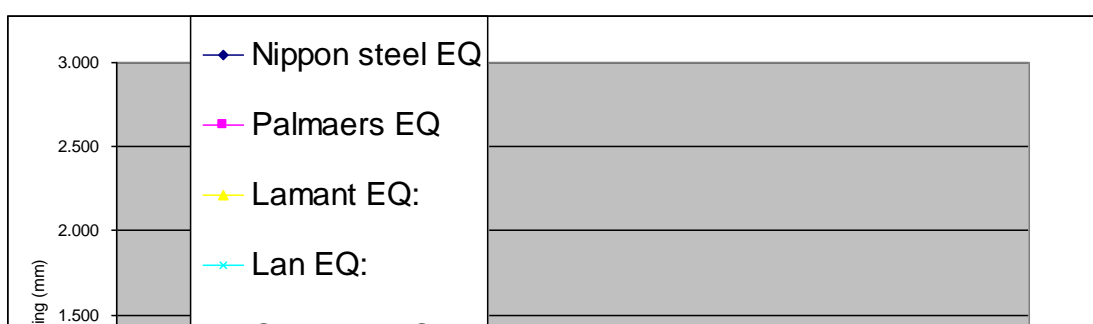
Fig **Error! Reference source not found.**.13 Buldging results from empirical equations

Table **Error! Reference source not found.**.2 shows the node id and the distance from center. We can get all the strains at different distance from center.

Table **Error! Reference source not found.**.2

node id	distance from center (mm)
514	0
450	20
418	30
354	50
258	80
130	120
2	160

node 2 shell thickness 0 mm

node 130 shell thickness 40 mm

node 258 shell thickness 80 mm

node 386 shell thickness 120 mm

node 450 shell thickness 140 mm

node 482 shell thickness 150 mm

node 514 shell thickness 160 mm
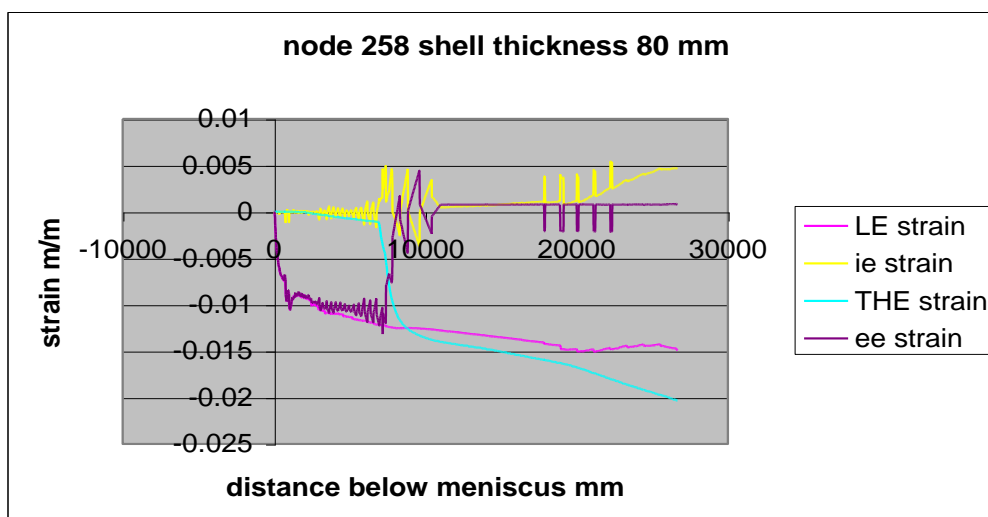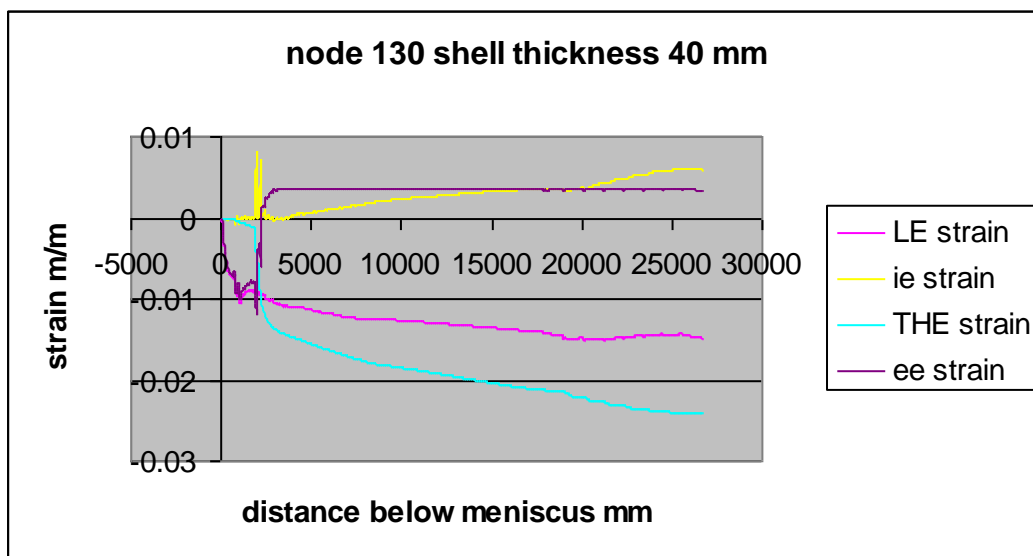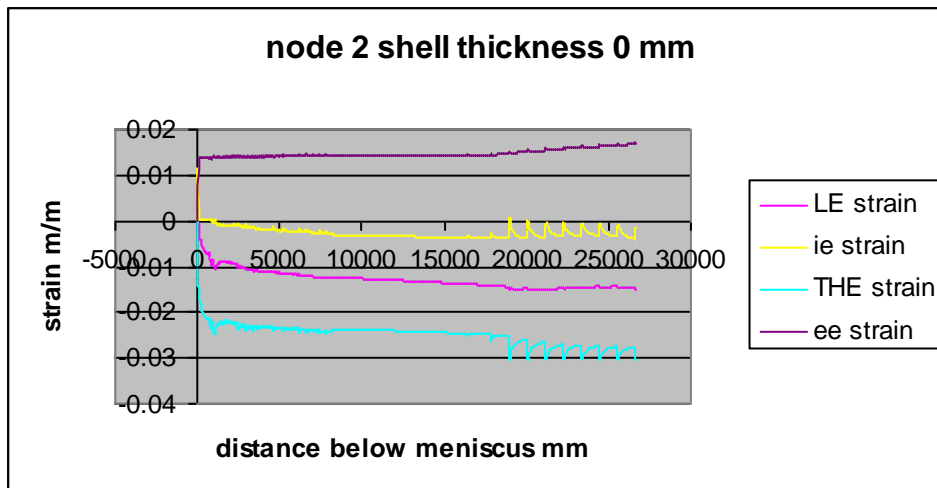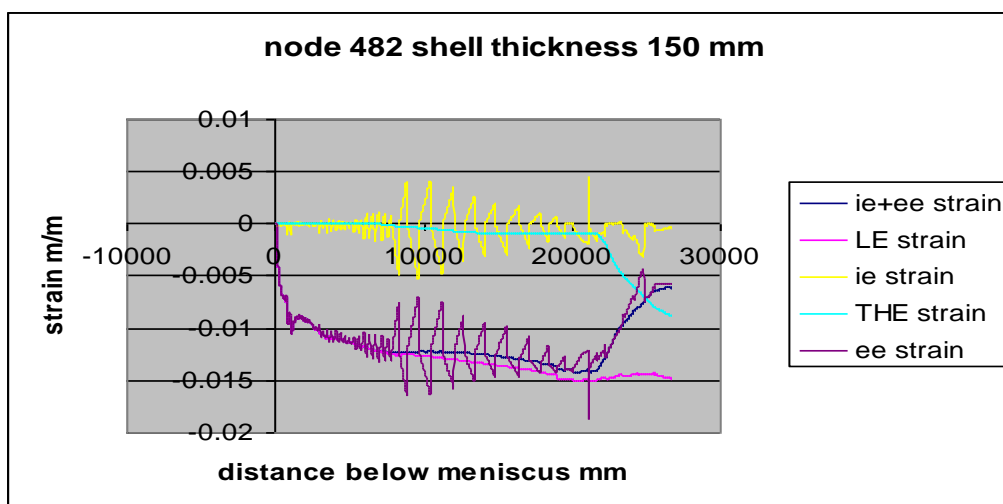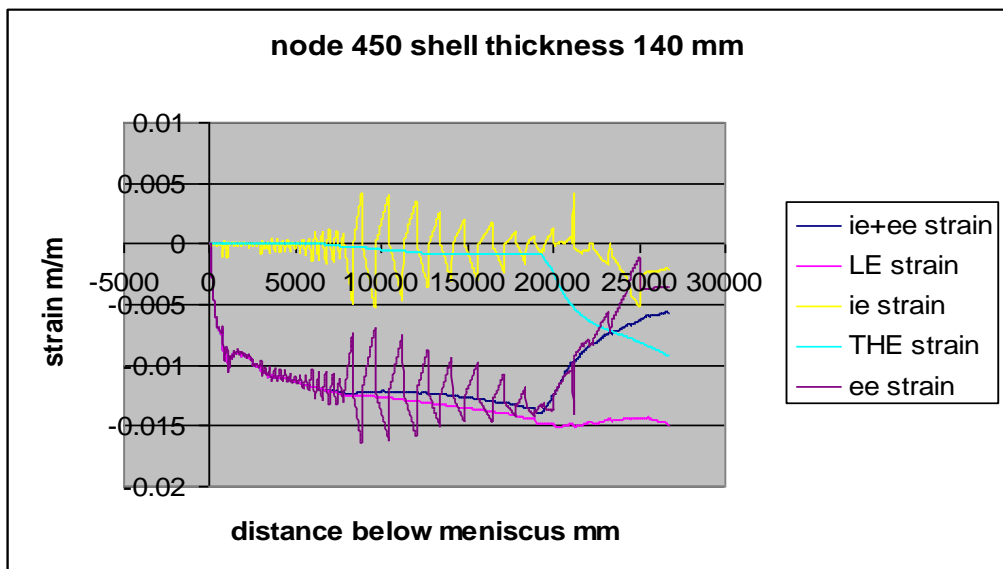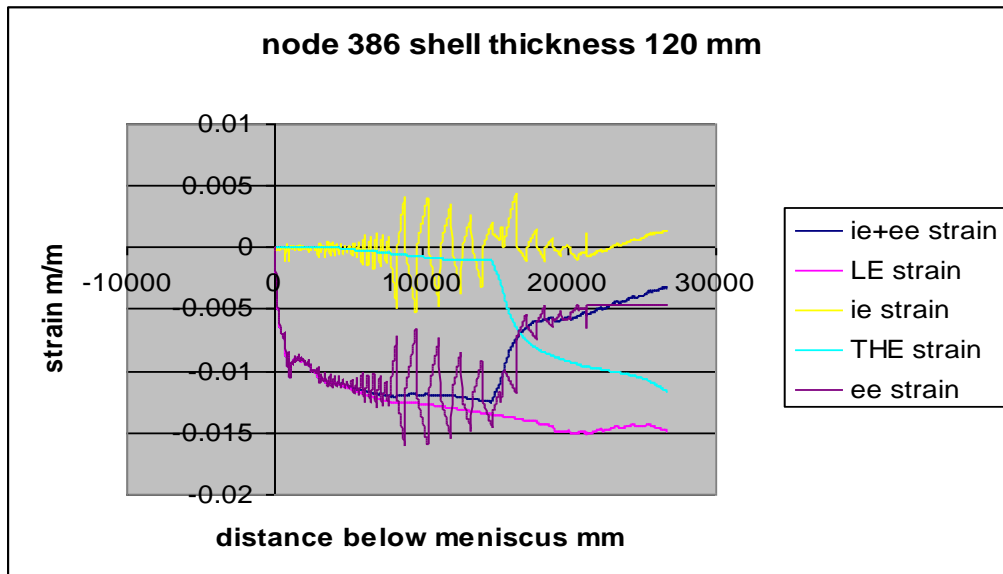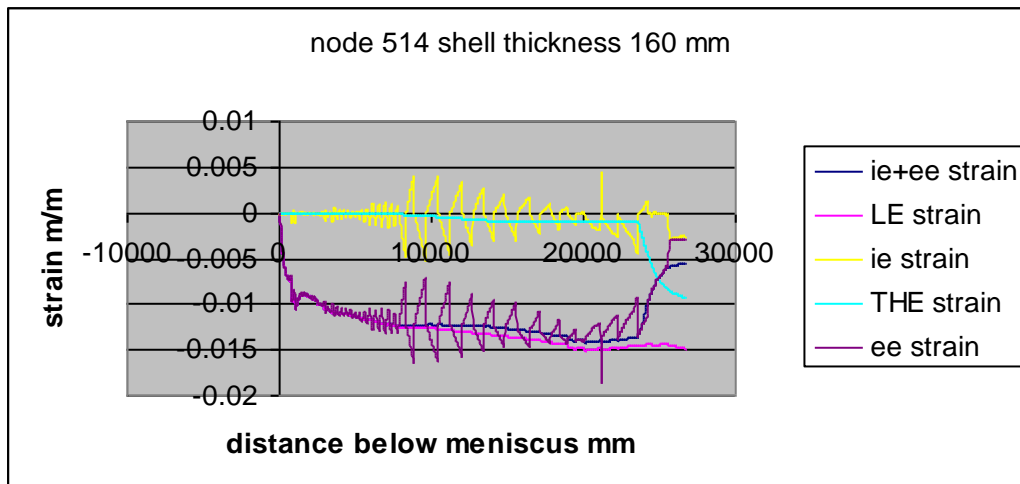
Fig **Error! Reference source not found.**.14   strain simulation at different shell thickness position.

Then we can get results Fig **Error! Reference source not found.**.15 as following: inelastic strain and shell thickness Vs distance below meniscus (mm). If the variation of ie strain from 90% solid fraction to 99% solid fraction in X coordinate is less than zero, the product is not susceptible to crack. Otherwise, crack sensibility increases.

t91
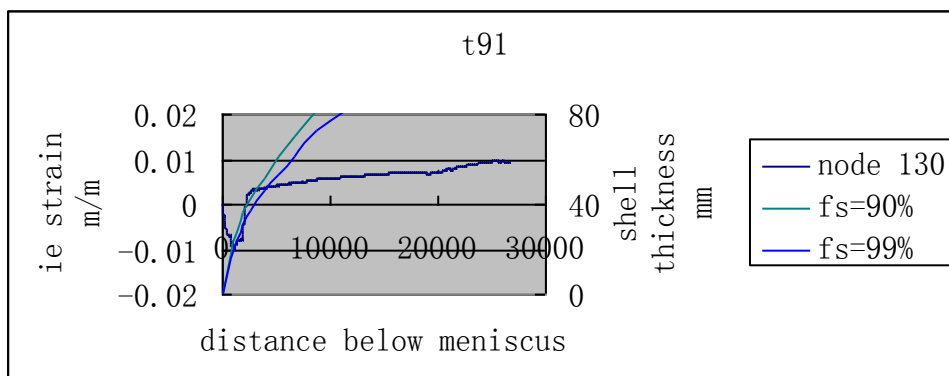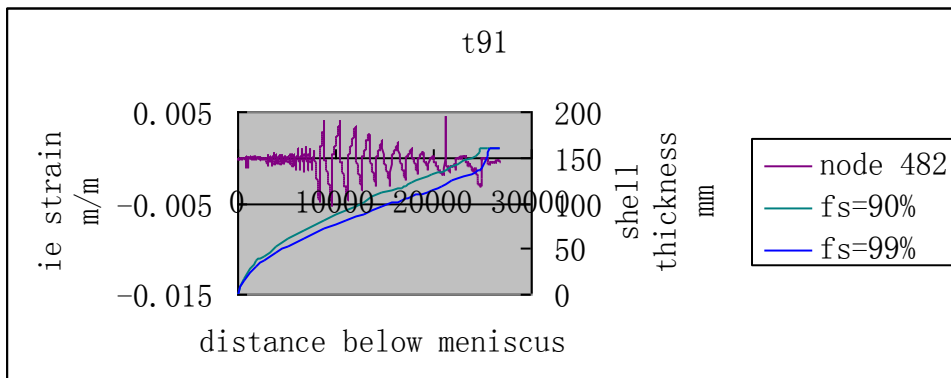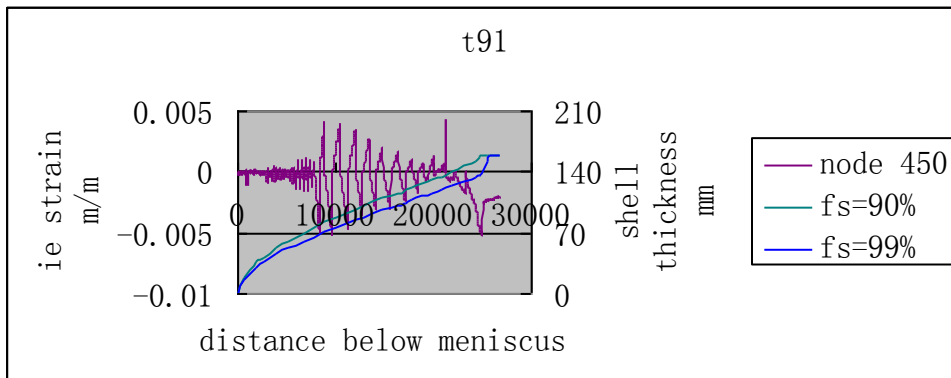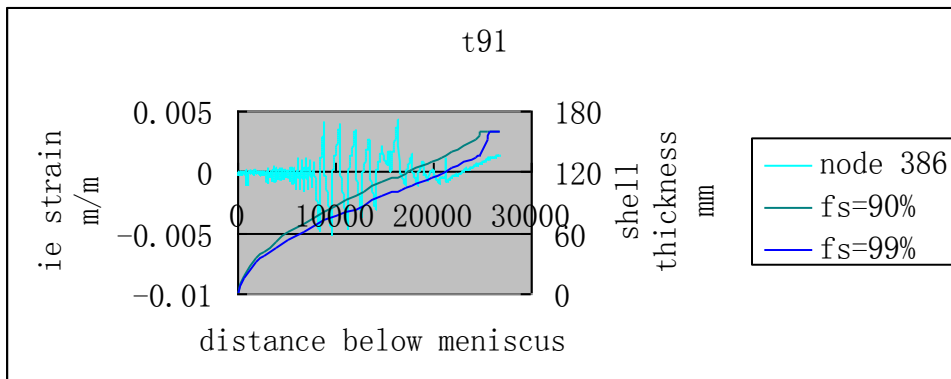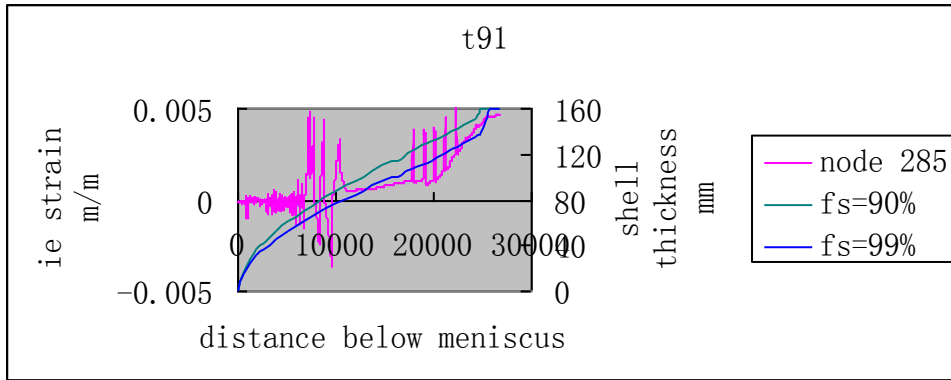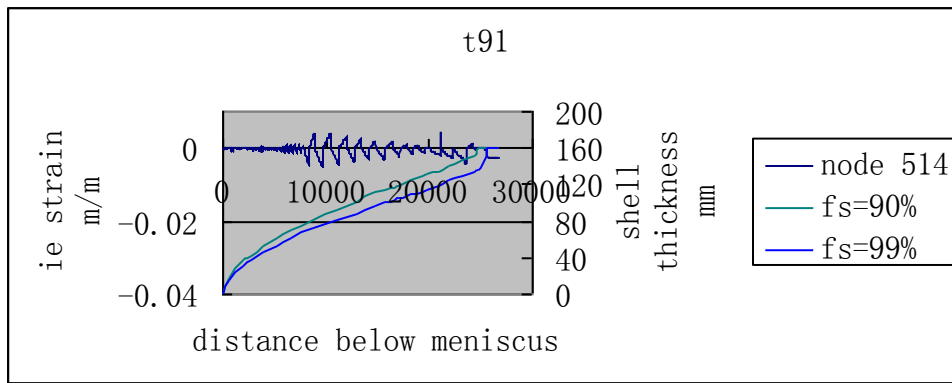
Fig **Error! Reference source not found.**.15 inelastic strain and shell thickness Vs distance below meniscus (mm).

Fig Error**! Reference source not found.**.16 shows the variation of inelastic strain from 90% fs to 99% fs at different shell thickness. From results we can see that the product is susceptible to crack about 10mm region from center. From thermal results, we know there is still liquid steel after the end of soft-reduction zone, which result in internal crack.
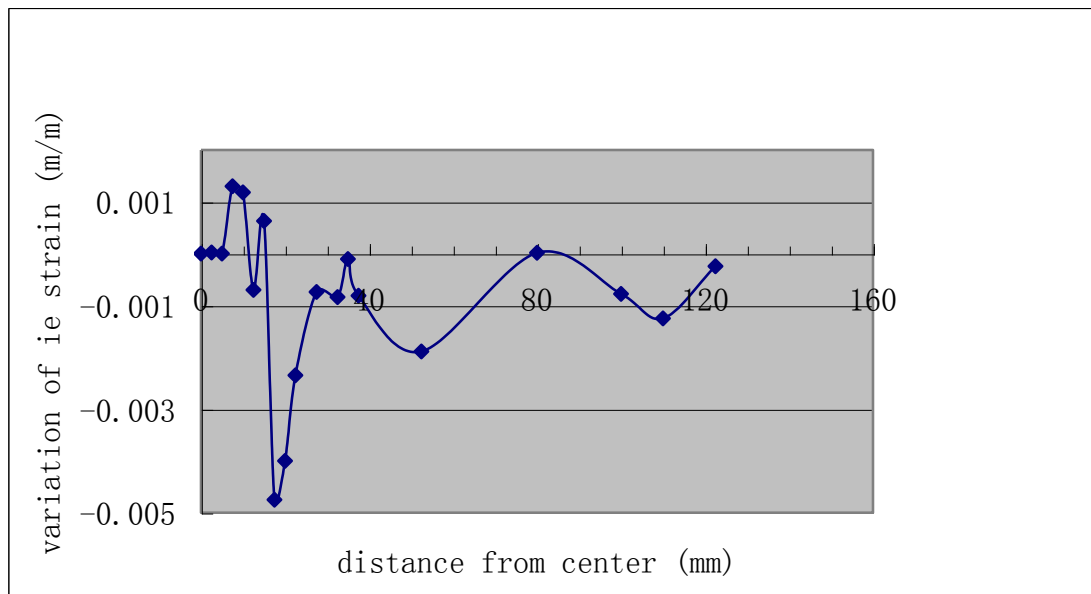
Fig **Error! Reference source not found.**.16 variation of inelastic strain from 90% fs to 99% fs

Fig **Error! Reference source not found.**.17 Sulfur print of T91

6.2.2 T92 steel

The T92 steel has been casted in Baosteel with 1550 C pour temperature and 0.55 m/min casting speed. The casting details are shown in T92 process specification. Fig **Error! Reference source not found.**.18and Fig **Error! Reference source not found.**.19show the heatflux of mold and film coefficient for calculation. Fig **Error! Reference source not found.**.20 shows the thermal simulation results by con1d and measurement results. They match not well.
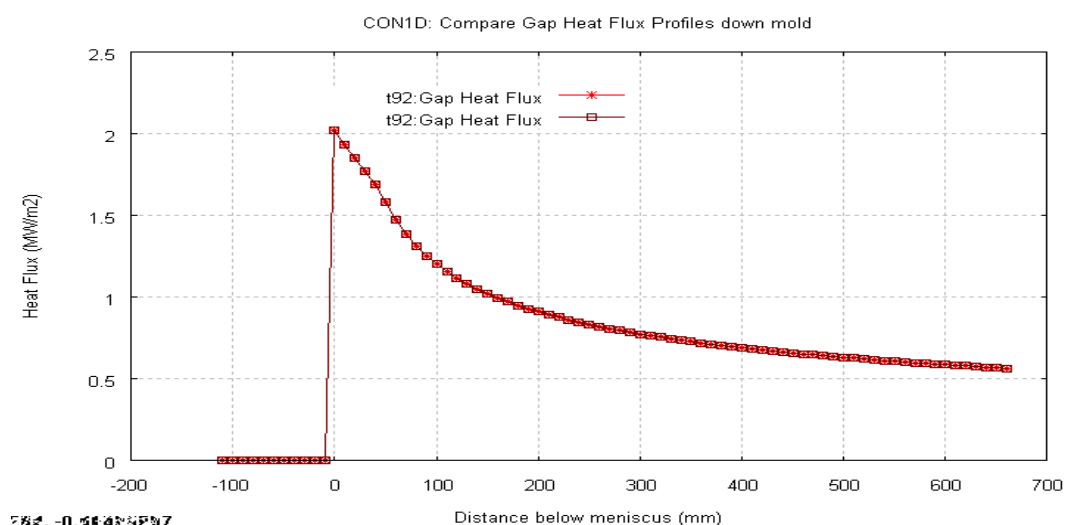
Fig **Error! Reference source not found.**.18 heatflux of mold
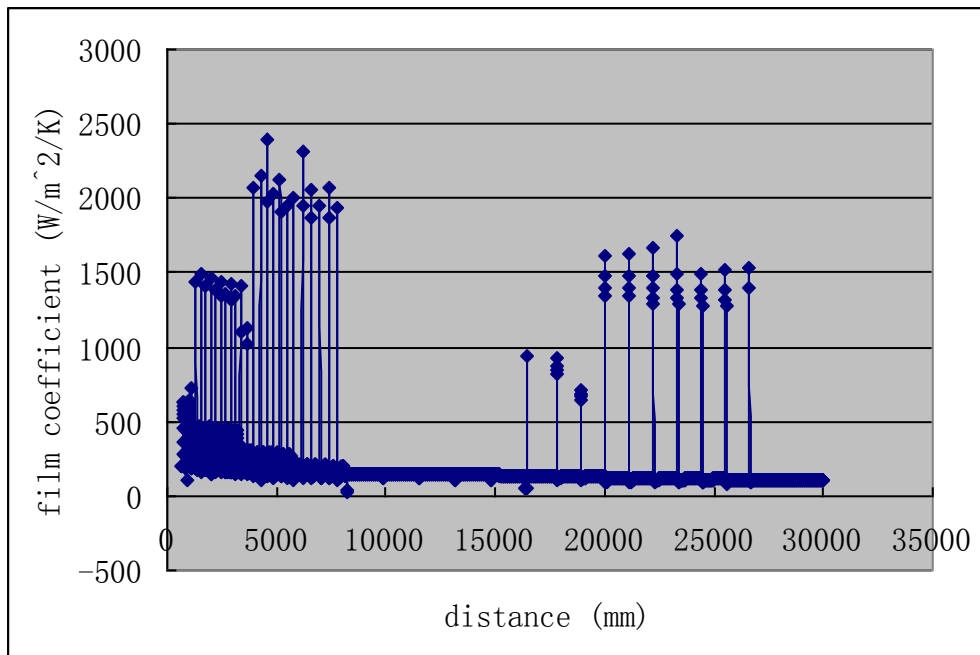
Fig **Error! Reference source not found.**.19 film coefficient

CON1D: Shell thickness and surface temperature in mold

23377.4 v= 1019.86 v2= 56.8636
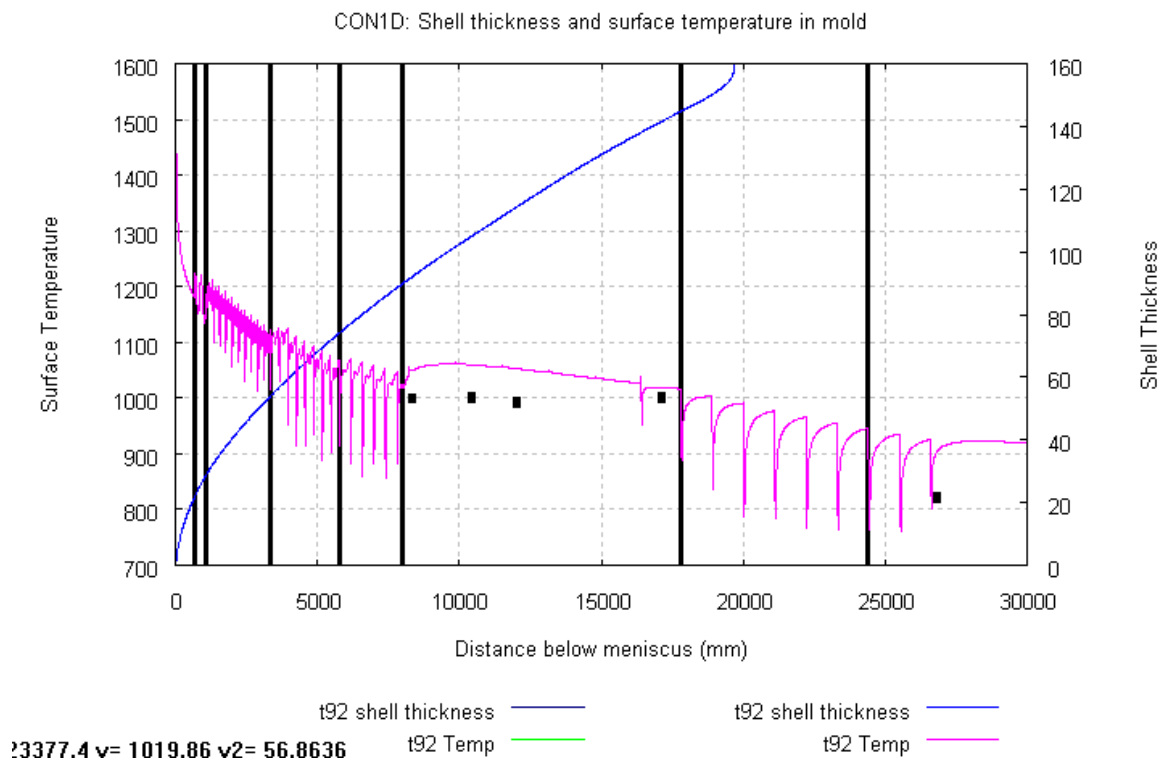
Fig **Error! Reference source not found.**.20 the thermal simulation results by con1d, and measurement results. Black square mean the measurement results.

Solid fraction, temperature distribution and temperature evolution of T92 is listed as following:
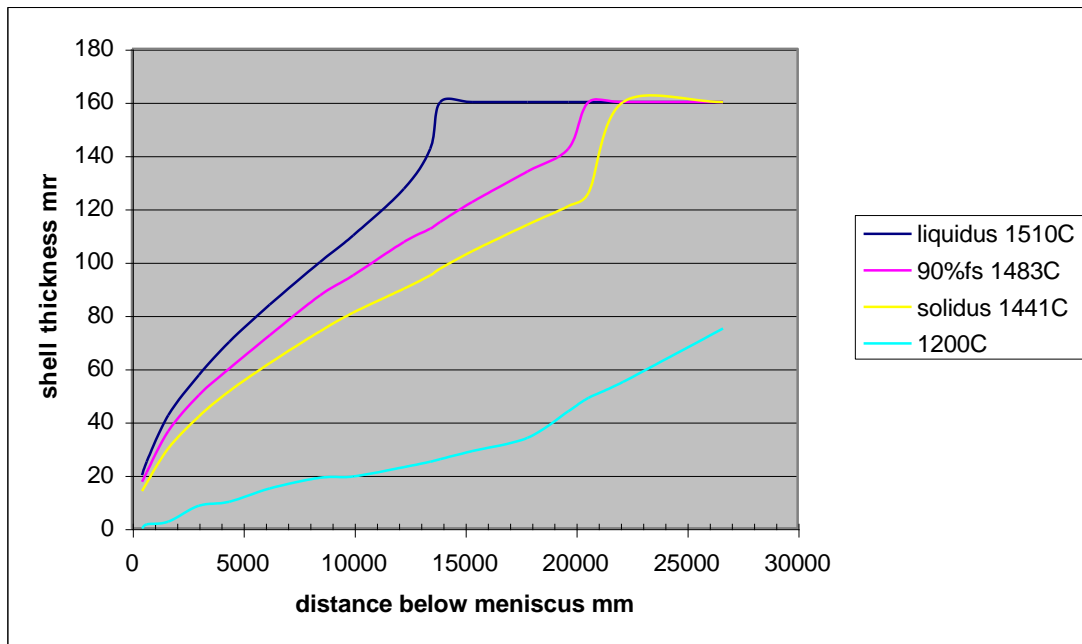
Fig **Error! Reference source not found.**.21 solid fraction of T92
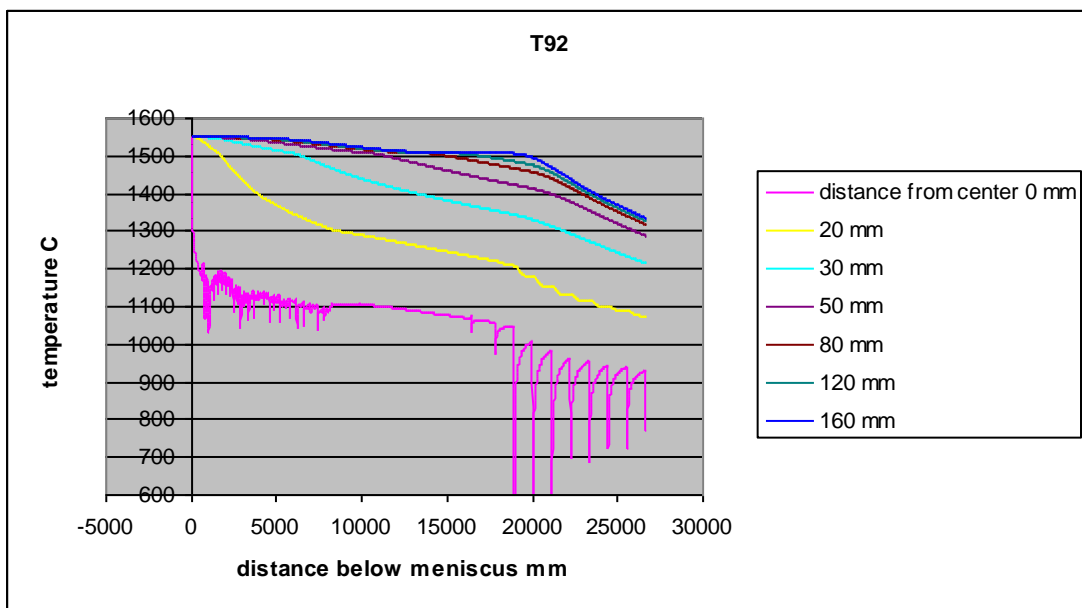
Fig **Error! Reference source not found.**.22 Calculated temperature distribution at different shell thickness in T92 by Abaqus model
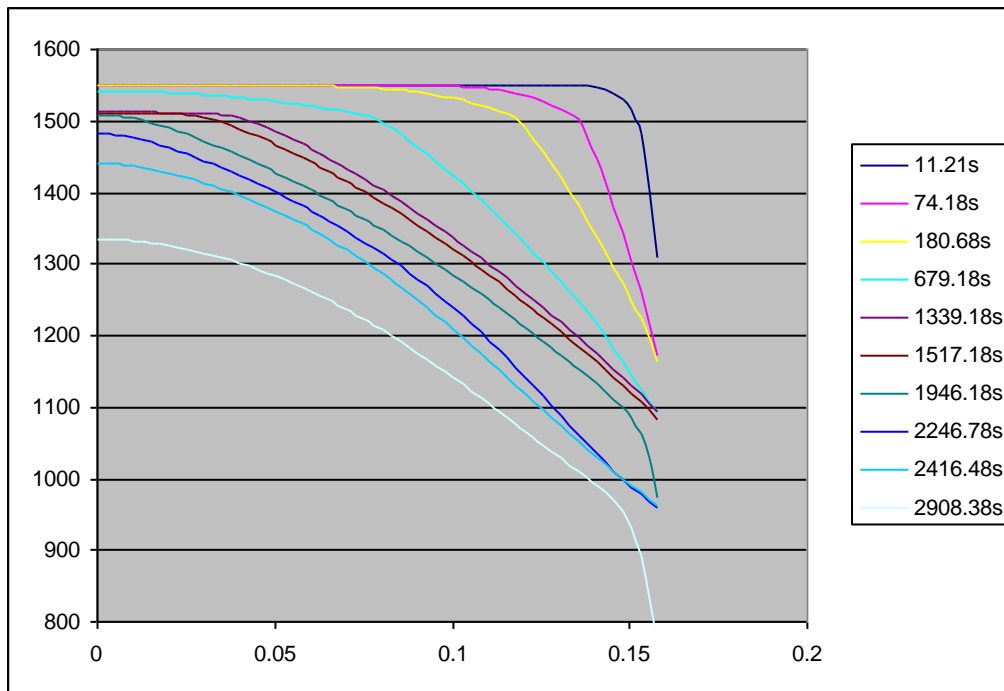
Fig **Error! Reference source not found.**.23 temperature evolution of T92

Fig **Error! Reference source not found.**.24 shows bulging results from empirical equations. We choose Lan equation results in our stress model.
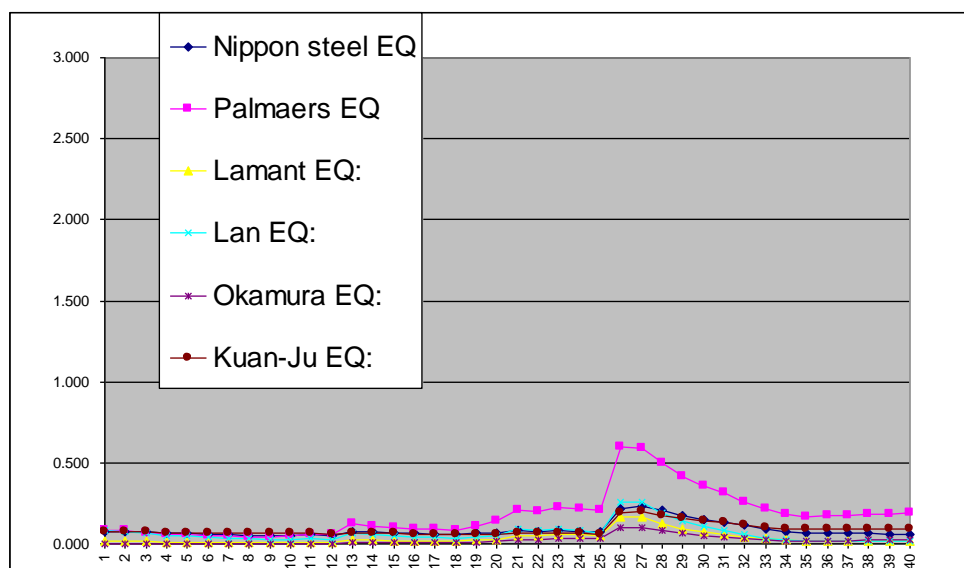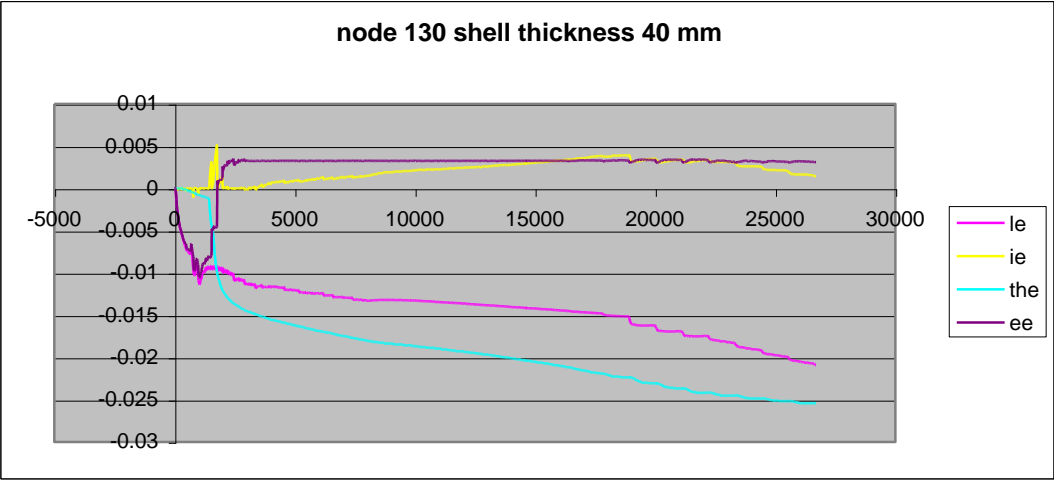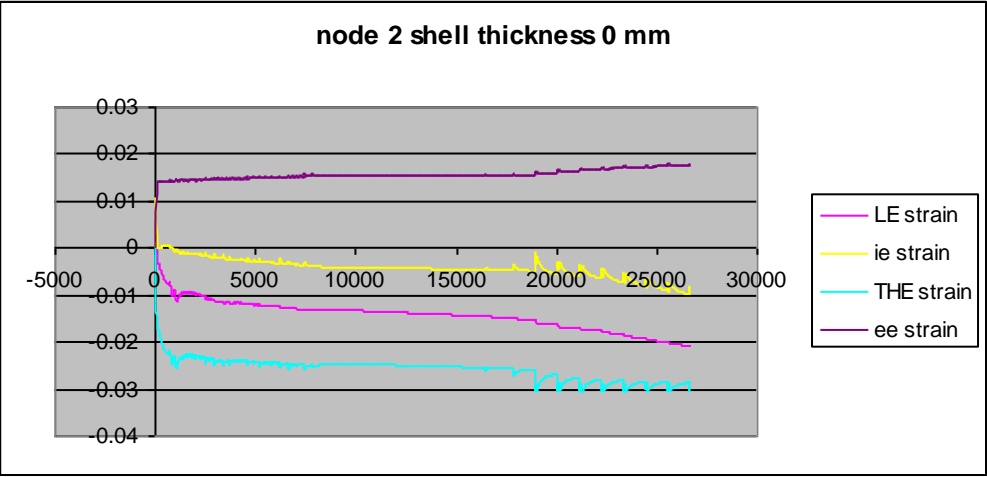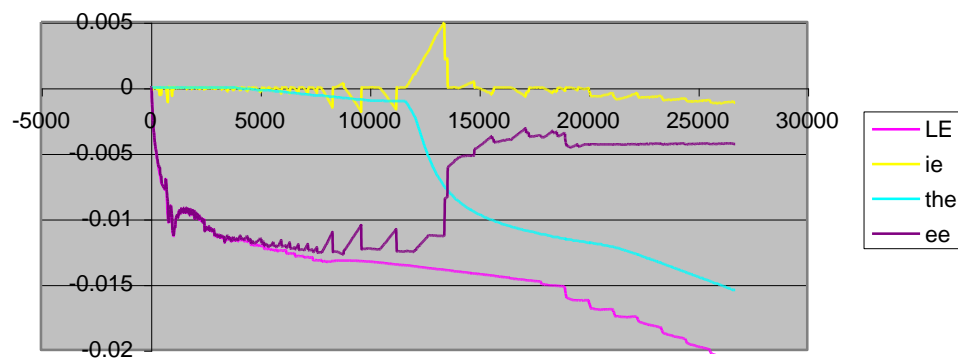

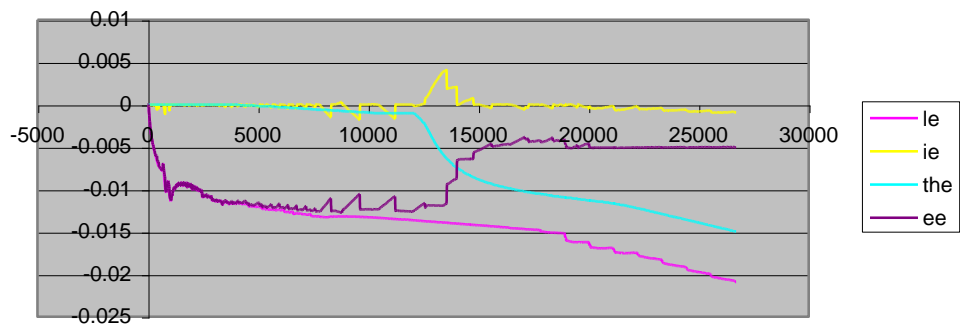Fig **Error! Reference source not found.**.24 Buldging results from empirical equations

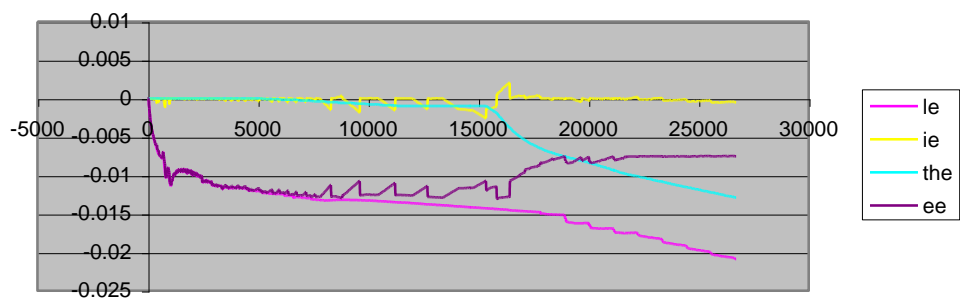All the strains at different distance from center calculated by Abaqus are listed as following:

node 2 shell thickness 0 mm

node 130 shell thickness 40 mm

node 258 shell thickness 80mm
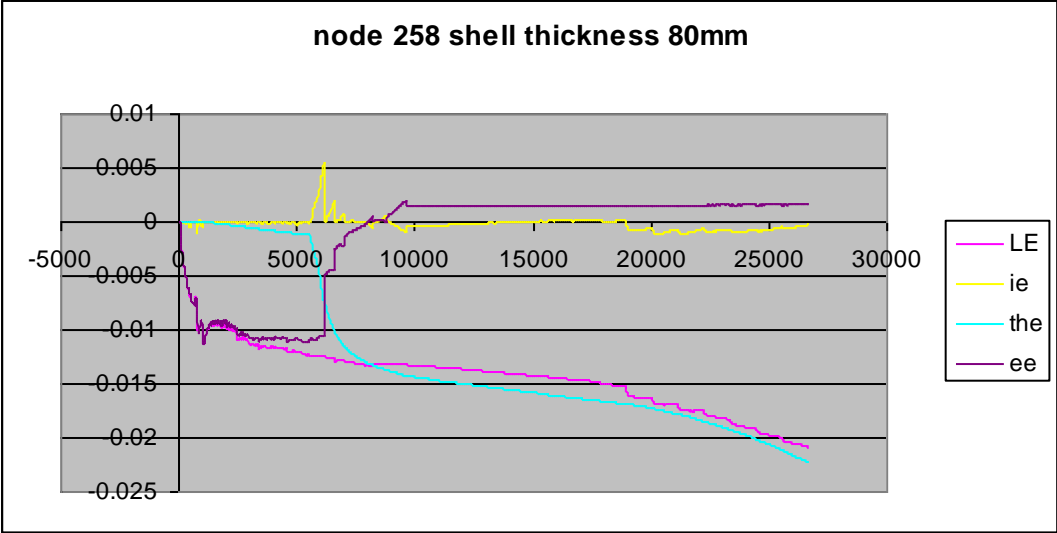
node 386 thickness 120 mm

node 394 thickness 122.5mm

node 450 thickness 140 mm
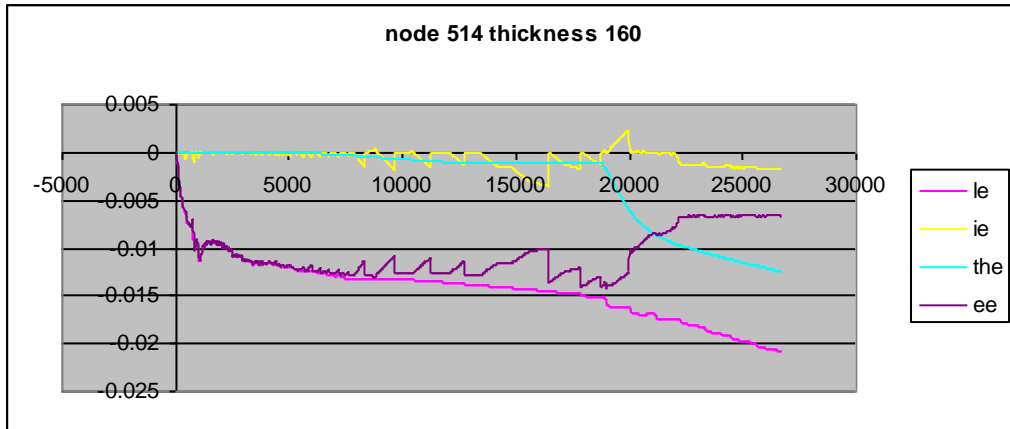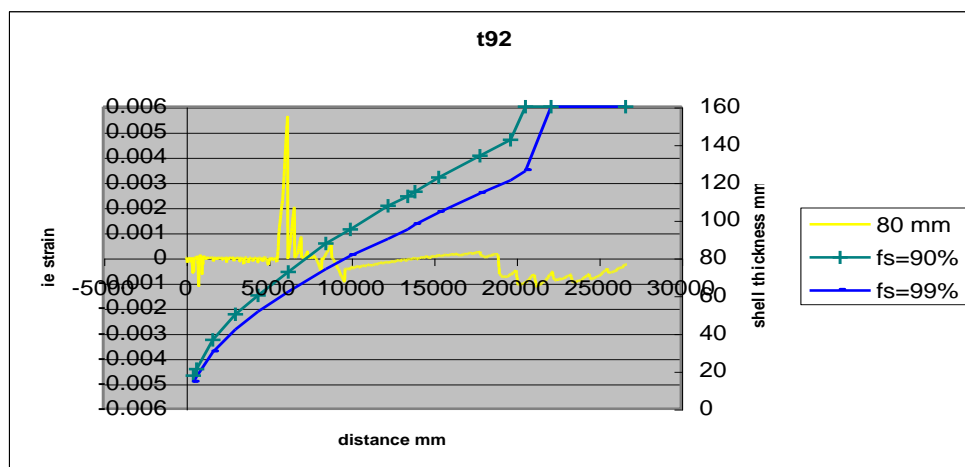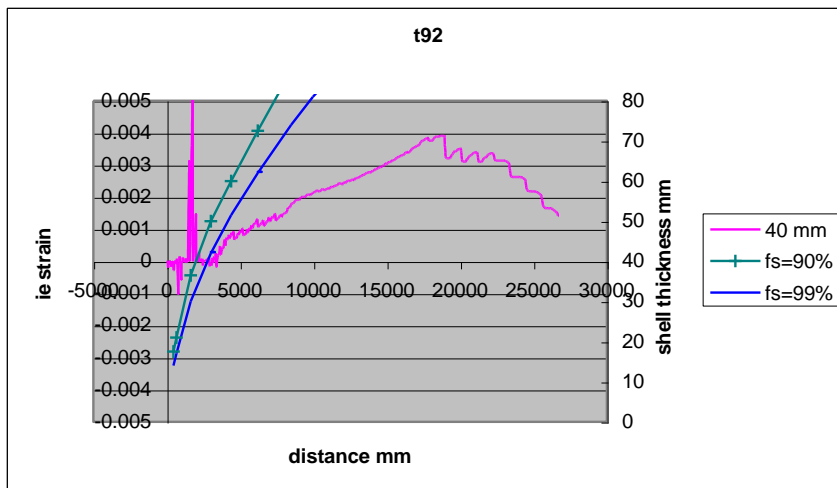
node 514 thickness 160

Fig **Error! Reference source not found.**.25 strains at different distance from center

Fig **Error! Reference source not found.**.26 shows inelastic strain and shell thickness Vs distance below meniscus (mm). If the variation of inelastic strain from 90% solid fraction to 99% solid fraction in the through-thickness direction is negative, the steel is in compression during its vulnerable period, so is not susceptible to hot-tear crack formation. If the strain accumulated over this temperature range is in tension, then crack sensitivity increases.
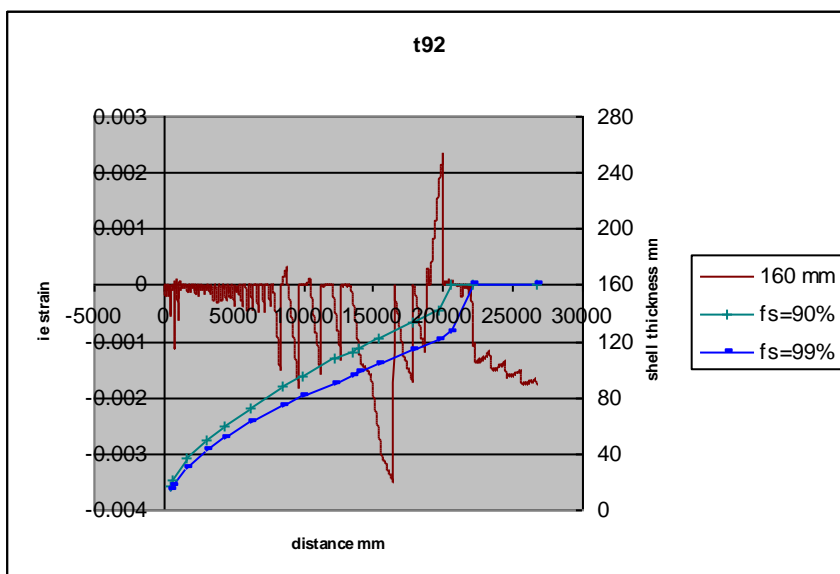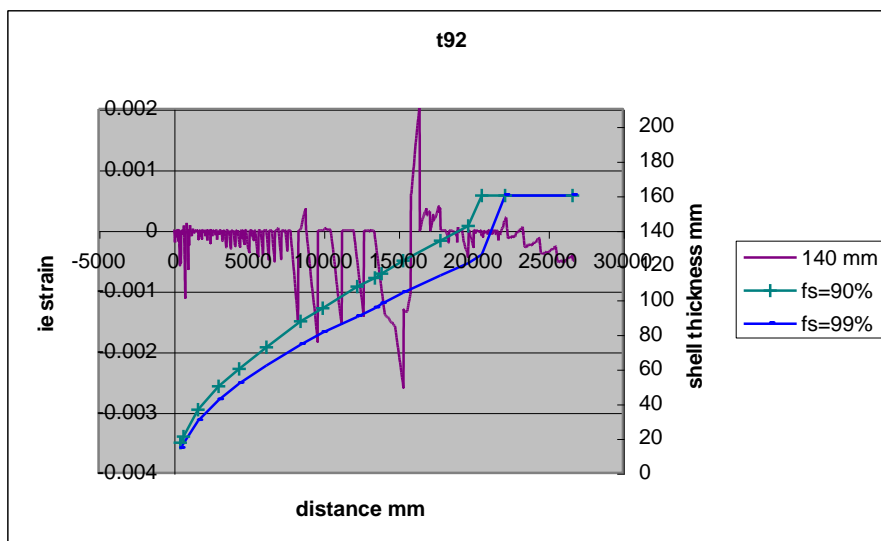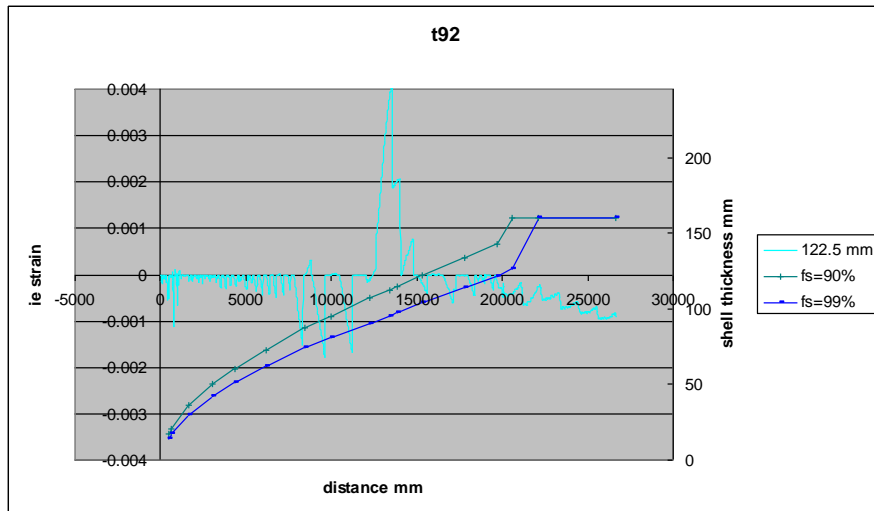

t92

t92

Fig **Error! Reference source not found.**.26 inelastic strain and shell thickness Vs distance

below meniscus (mm)

Fig Error**! Reference source not found.**.27 shows the variation of inelastic strain from 90% fs to 99% fs at different shell thicknesses. From results we can see that the product is susceptible to crack about 40mm region from center. Thus, cracks are likely at this location during spay cooling. The entire exterior from 50mm to the surface is in compression.
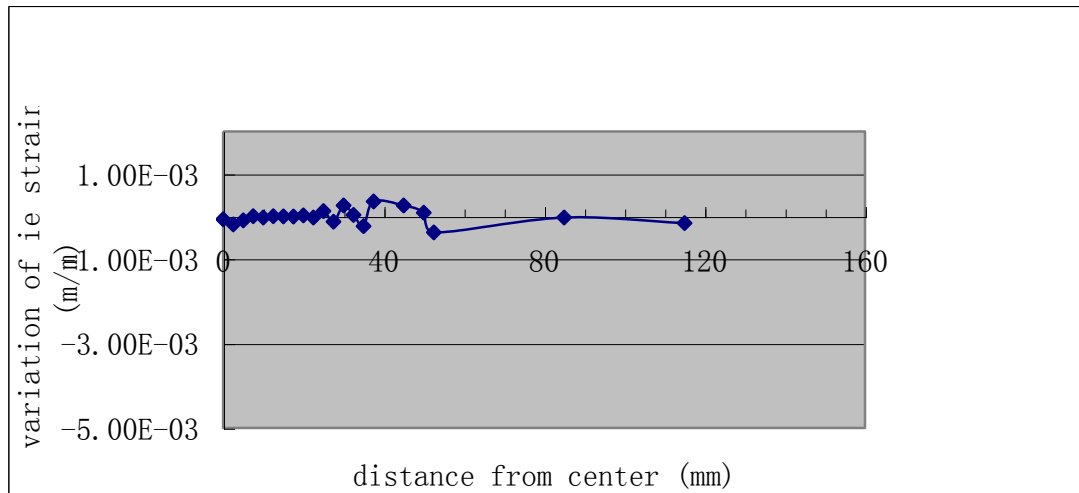

Fig **Error! Reference source not found.**.27 the variation of inelastic strain from 90% fs to 99% fs at different shell thickness.
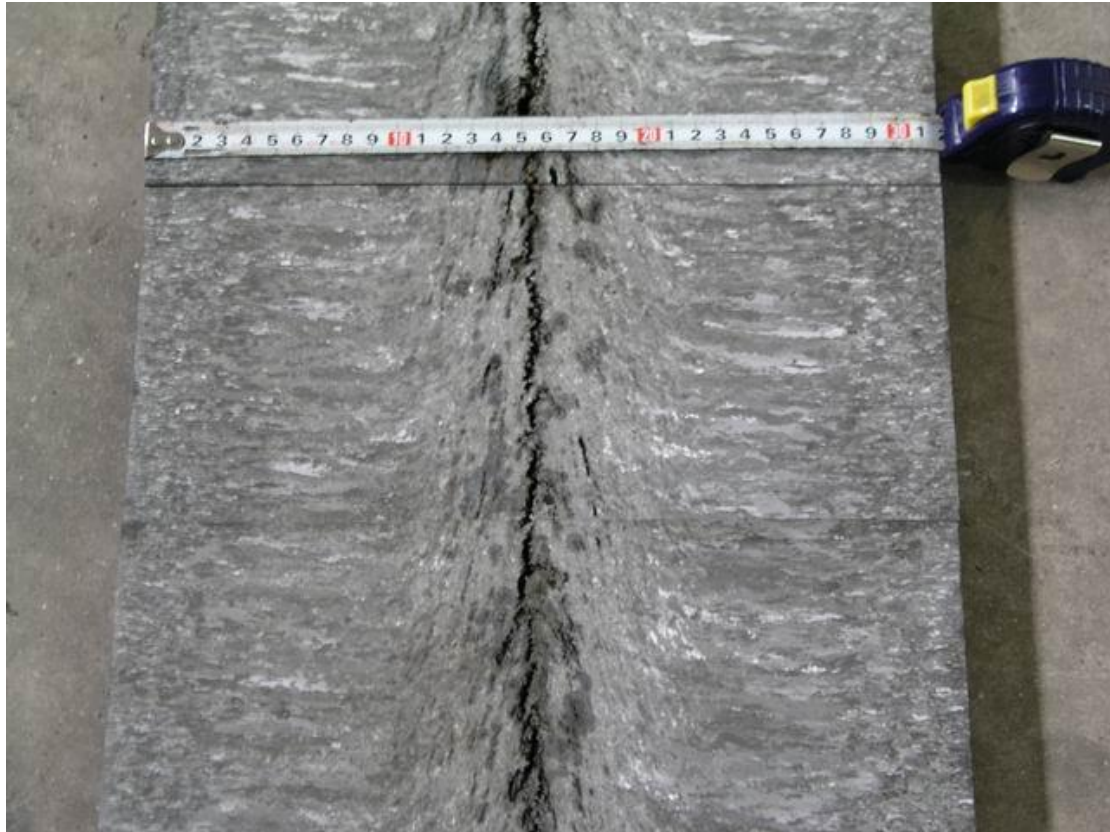
Fig **Error! Reference source not found.**.28 sulfur print of T92, showing centerline crack defects

7. Conclusion

1. A thermal and stress model of the continuous bloom caster at Baosteel has been developed, and validated with analytical solutions. The profiles of temperature have been simulated and validated with plant measurements for both T91 and T92.
2. Simulations of strain and stress on T91 and T92 have been simulated, based on the temperature predictions.
3. The mechanism of centerline cracks appears to be from hot tear crack formation of T91 and T92, based on shrinkage and net tensile strain predicted near the time of final solidification.
4. From simulation results, carefully-located soft-reduction is a promising direction to decrease internal crack. Careful control of low pouring temperature is also recommended.

8. References

[1] J. K. Brimacombe: Crack Formation in the Continuous Casting of Steel. Metallurgical Transaction B, 1977, vol. 8B, pp. 489-505.

[2] H. Mori: Tetsu To Hagane, 1972, vol. 58, pp. 1511-34.

[3] H. Mori: Tetsu To Hagane, 1974, vol. 60, pp. 784-93.

[4] W. T. Lankford: Met. Trans., 1972, vol. 3, pp. 1331-57.

[5] C. J. Adams: Open Hearth Proc., 1971, vol. 5, pp. 290-302.

[6] A. Fuchs: ESTEL-Berichte aus Forschung und Entwicklung unserer werke, 1975, no. 3, pp. 127-35.

[7] Y. Lida, H. Moriwaki, T. Ueda, and Y. Habu: Tetsu To Hagane, 1973, Vol. 59, p. S89.

[8] S. Hasabe, T. Koga, T. Yamura, and Y. Sugikawa: Tetsu To Hagane, 1972, vol. 58, P. 522.

[9] J. L. Robbins, O. C. Shepard, and O. D. Sherby: Trans. ASM, 1967, vol. 60, pp. 205-16.

[10] E. A. Mizikar: Trans. TMS-AIME 1967, vol. 239 (11), pp. 1747-58.

[11] J. E. Lait, J. K. Brimacombe, and F. Weinberg: Ironmaking and Steelmaking, 1974, vol. 1(2), pp. 90-97.

[12] E. A. Upton, T. R. S. Rao, P. H. Dauby, and R. C. Knechtges: Iron steel-maker, 1988, vol. 15(5),   pp. 51-57.

[13] R. Davies, N. Blake, and P. Campbell: 4th Int. conf. Continuous Casting, Preprint vol. 2, Brussels, Belgium, 17-19 May, 1988, VS, Dusseldorf, FRG, 1988, vol. 2, pp. 645-54

[14] R. B. Mahapatra, J. K. Brimacombe, I. V. Samarasekera, N. Walker, E. A. Paterson, and J. D. Young: Metall. Trans. B, 1991, vol. 22B, pp. 861-74.

[15] J. K. Brimacombe: Can. Metall. Q., 1976, vol. 15 (2), pp.   163-75.

[16] A. Mooitra and B. G. Thomas:76th Steelmaking Conf., Dallas, TX, 28-31 Mar., 1993, ISS, Warrendale, PA, 1993, vol. 76, pp. 657-67

[17] M. R. Aboutalebi, R. I. L. Guthrie, and M. Hasan: Steel Res., 1994, vol. 65 (6), pp. 225-33

[18] F. Wimmer, H. Thome, and B. Lindorfer: Berg. Huttenmanische Monatshefte, 1996, vol. 141 (5), pp. 185-91.

[19] H. Nam, H. S. Park, and J. K. Yoon: Iron Steel Inst. Jpn. Int., 2000, vol. 40 (9), pp. 886-92.

[20] J. E. Lee, T. J. Yeo, K. H. Oh, J. K. Yoon, and U. S. Yoon: Metall. Mater. Trans. A, 2000, pp. 769-76.

[21] B. G. Thomas, W. R. Storkman, and A. Moitra: IISC 6th Int. Iron and Steel Congr., Nagoya, Japan, 21-26 Oct., 1990, ISIJ, Tokyo, Japan, 1990, vol 3, Steelmaking I, pp. 348-55.

[22] C. Li and B. G. Thomas: Brimacombe Memorial Symp., Vancouver, BC, Canada, 1-4 Oct., 2000, CIMMP, Montreal, PQ, Canada, 2000, pp. 595-611.

[23] B. G. Thomas, A. Moitra, and R. McDavid: Iron Steelmarker, 1996, vol. 23 (4), pp. 57-70.

[24] X. Huang, B. G. Thomas, and F. M. Najjar: Metall. Mater. Trans. B 1992, vol. 23B, pp. 339-56.

[25] C. A. Sleicher and M. W. Rouse, Int. J. Heat Mass Transf. 1975, vol. 18, pp. 677-83,

[26] Nozaki, T., Matsuno, J., Murata, K., Ooi, H., Kodama, M., "A Secondary Cooling Pattern for Preventing Surface Cracks of Continuous Casting Slab", Trans. ISIJ, 1978, vol. 18, pp.330-338

[27] P.F. Kozlowski, B.G. Thomas, J.A. Azzi, and H. Wang, Simple constitutive equations for steel at high temperature, Met. Mat. Tran. A, Vol. 23, 903-918, 1992

[28] Zhu H., Coupled thermal-mechanical FE model with application to initial solidification, Ph.D. Thesis, University of Illinois   1993

[29] S. Koric and B.G. Thomas, Efficient Thermo-Mechanical Model for Solidification Processes, International Journal for Num. Methods in Eng. Vol. **66** 1955-1989, 2006

[30] Abaqus User's Manual 6.8, Dassault Sys., 2008

[31] G. Li: Ph. D. Thesis, University of Illinois, Urbana, IL, 1996.

[32] B. G. Thomas and T. Morthland: "3-D Heat Transfer Analysis of Columbus Slab Casting Mold," CCC Report 2001, Univ. of Ill., Urban, IL.

[33] D. R. Poirier and G. H. Geiger: Transport Phenomena in Materials Processing, TMS, Warrendaler, PA, 1994, p.339.

[34] Y. Meng and B. G. Thomas: Metallurgical and Materials Transaction B, 2003, vol. 34B, pp. 685-705.

[35] J. H. Weiner and B. A. Boley. Elasto-plastic thermal stresses in a solidifying body. Journal of the Mechanics and Physics of Solids 1963; 11:145-154.

[36] C. Li and B. G. Thomas. Thermo-mechanical finite-element model of shell behaviour in continuous casting of steel. Metallurgical and Materials Transactions B 2004; 35B(6): 1151-1172.

[37] K. Harste, A. Jablonka, and K. Schwerdtfeger: 4th Int. Conf. Continuous Casting, Brussels. Belgium, Verlag Stahleisen, Dusseldorf 1988, vol. 2, pp. 633-44

[38] I. Jimbo and A. A. W. Cramb: Metall. Trans. B, 1993, vol. 24B, pp. 5-10.